


Drone Detection and Tracking in Real-Time by Fusion of Different Sensing Modalities

Fredrik Svanström ^{1,†}, Fernando Alonso-Fernandez ^{2,*}  0000-0002-1400-346X and Cristofer Englund ^{2,3,‡}

¹ Air Defence Regiment. Swedish Armed Forces

² School of Information Technology, Halmstad University, SE 301 18 Halmstad, Sweden

³ RISE, Lindholmspiren 3A, SE 417 56 Gothenburg, Sweden

* Correspondence: feralo@hh.se

† Email: DroneDetectionThesis@gmail.com

‡ Email: cristofer.englund@hh.se

Abstract: Automatic detection of flying drones is a key issue where its presence, specially if unauthorized, can create risky situations or compromise security. Here, we design and evaluate a multi-sensor drone detection system. In conjunction with common video cameras and microphone sensors, we explore the use of thermal infrared cameras, pointed out as a feasible and promising solution that is scarcely addressed in the related literature. Our solution integrates a fish-eye camera as well to monitor a wider part of the sky and steer the other cameras towards objects of interest. The sensing solutions are complemented with an ADS-B receiver, a GPS receiver, and a radar module, although the latter has been not included in our final deployment due to its limited detection range. The thermal camera is shown to be a feasible solution as good as the video camera, even if the camera employed here has a lower resolution. Two other novelties of our work are the creation of a new public dataset of multi-sensor annotated data that expand the number of classes in comparison to existing ones, as well as the study of the detector performance as a function of the sensor-to-target distance. Sensor fusion is also explored, showing that the system can be made more robust in this way, mitigating false detections of the individual sensors.

Keywords: Drone detection, UAV detection, Anti-drone systems

1. Introduction

Drones, also referred to small and remotely controlled unmanned aerial vehicles (UAVs), can fulfil valuable societal roles such as law enforcement, medical, construction, search and rescue, parcel delivery, remote area exploration, topographic mapping, forest/water management, or inspection of big infrastructures like power grids [1]. Their low cost and ease of operation has caused that drones have also found their way into consumer use just for recreation and entertainment [2]. Unfortunately, they can also be intentionally or unintentionally misused, so that safety of others can be threatened. For example, an aircraft can be severely damaged if it collides with a consumer-sized drone, even at moderate speeds [3], and an ingested drone can rapidly disable an aircraft engine. An increasingly common risk is the report of drone sightings in restricted airport areas which ultimately has led to total closure of the airport and cancellation of hundreds of flights [4]. Several near-misses and verified collisions with UAVs have involved hobbyist drone operators flying in violation of aviation safety regulations, sometimes without knowledge about such violation. This rapid development in the use and potential misuse of UAVs has consequently produced an increase in research on drone detection [5,6] to counteract potential risks due to intrusion in restricted areas, either intentional or unintentional.

Received:

Accepted:

Published:

Publisher's Note: MDPI stays neutral with regard to jurisdictional claims in published maps and institutional affiliations.

Copyright: © 2022 by the authors. Submitted to *Drones* for possible open access publication under the terms and conditions of the Creative Commons Attribution (CC BY) license (<https://creativecommons.org/licenses/by/4.0/>).

In this work, we address the design and evaluation of an automatic multi-sensor drone detection and tracking system. Our developments are built on state-of-the-art machine learning techniques, with methods extended from conclusions and recommendations from the related literature [5,7]. In addition to effective detection, classification and tracking methods, the existing literature also points out sensor fusion as an important open area to achieve more accuracy and robustness compared to a single sensor. Despite this, research in sensor fusion for drone detection is scarce [7–10]. Our work also encompasses the collection and annotation of a public dataset to accomplish training and evaluation of the system. The lack of public reference databases that serve as benchmark for researchers is identified as another fundamental challenge [5]. Three different consumer-grade drones are included in the dataset together with birds, airplanes and helicopters, in which constitutes the published dataset with the biggest number of target classes (drone, bird, airplane and helicopter, in comparison to others which only contain three, two or one of these classes only). To achieve effective detection of drones, in building the classes, we have considered the inclusion of other flying objects that are likely to be mistaken for a drone [11,12]. Another missing piece in previous studies that we address here is the classification performance of the system as a function of the distance to the target, with annotations of the database including such information as well.

A preliminary version of this article appeared at a conference [13]. In the present contribution, we substantially increase the amount of reported results, e.g. the previous paper only reported the precision, recall and F1-score of the individual sensors provided in Tables 3, 6 and 9, as well as the fusion results of Figure 22. Here, we extensively analyze the effect of internal parameters of the different detectors on their performance for the different sensors. We also report results with a radar module and provide comments about the fish-eye camera motion detector, all of them missing in the previous publication. Additional results on the fusion of sensors are also provided, including an Appendix with complementary observations and visual examples. New detailed information about the system architecture, hardware and software employed is also provided, including details about implementation and design choices not included in the previous publication. The related work is also described in more detail.

The rest of the paper is organized as follows. Section 2 describes related work. Section 3 extensively describes the proposed system, including the architecture, the hardware components, the involved software, the Graphical User Interface, and the dataset. The experimental results are presented and discussed in Section 4. Finally, the conclusions are given in Section 5.

2. Related Work

To automatically detect flying drones, some form of sensor system is needed. As shown in [8], the fusion of data from multiple sensors to achieve more accurate results than derived from single sensors, while compensating for their individual weaknesses, is well-founded when it comes to the drone detection task. The sensors that may be considered, and hence can be found in the related scientific literature, are: *i*) radar (on several different frequency bands and both active and passive), *ii*) cameras in the visible spectrum, *iii*) cameras detecting thermal infrared emission (IR), *iv*) microphones for the detection of acoustic vibrations, i.e. sound, *v*) sensors to detect radio frequency signals to and from the drone and the drone controller (RF), and *vi*) scanning lasers (Lidar). As mentioned in [8] and explored further in [14], even humans are used to do the task. It has also been successfully demonstrated that animals can be trained to fulfil an anti-drone role [15]. Systems for drone detection utilizing one or more of the aforementioned sensors may also be combined with some form of effector to try to bring the flying drone down or, in some other way, take control of it. An effector component, however, is not part of this work.

An introduction to the subject of drone detection can be found in [7], published in 2018. It contains a comparison of advantages and disadvantages of different drone detection and

tracking techniques. Regarding sensor fusion, the authors state that “For accurate and quick detection/tracking of UAVs, data fusion techniques that can simultaneously use information from multiple types of sensors carry critical importance, and this constitutes an open research area”. One of the conclusions of [7] is also that “Future research directions include developing effective machine learning methods for detecting, classifying, and tracking drones in various scenarios of interest”. The paper also briefly provides an overview of ways to interdict unauthorized drones.

The paper [5] presents a comprehensive review of the literature on machine learning for drone detection and classification. Published in 2019, it summarizes the results of about 50 references based on the type of sensor, describing the specifications and limitations of the different techniques. The authors stress on more than one occasion the lack of publicly available reference datasets. Furthermore, they also write that “No study was presented which investigated the classification performance as a function of drone distance not to speak of determining the range using regression models”, a direction which is pinpointed as “very interesting”. They also highlight that most of the research in drone detection using visual sensors do not specify the sensing device, drone type, detection range, or dataset used, all being key aspects to make works reproducible.

Also published in 2019, the paper [8] has an exhaustive 178 references. Within these, there are not only articles specific to drone detection and classification, but also regarding the general techniques employed, e.g. useful aspects of sensor fusion and machine learning. It emphasizes as well the lack of works tackling UAV detection and classification using thermal cameras, despite the successful use of such sensors together with deep learning-based methods for general object detection. As such, the authors motivate researchers to “turn their attention to this novel subject”.

2.1. Thermal Infrared Sensors

The work described in [16], from 2017, does not utilize any form of machine learning. Instead, detection and classification is done by a human in real-time looking at the output video stream. The sensor used is a low-cost FLIR Lepton 80×60 pixels thermal camera. Connected to a Raspberry Pi, the authors are able to detect three different drone types up to a distance of 100m. One of the things the paper mentions is that it is the drone battery and not the motors (as one may presume), that is the most significant source of heat radiation. With the background from this paper and the ones above, the present work will try to extend these findings using a higher resolution sensor (FLIR Boson with 320×256 pixels) in combination with machine learning methods to build a system that automatically detects, classifies and tracks drones. The IR-camera will also be combined with at least one additional sensor.

The possible advantages of using not only video in the visible range but also a thermal infrared camera are explored to some extent in [17]. In the paper, from 2019, the authors describe how they combine the sensors with deep-learning-based detection and tracking modules. The IR-videos used are stated to have a resolution of 1920×1080 , but unfortunately, the sensor is not specified in any detail. To detect the drones, a Faster-RCNN is implemented and given the difficulties of acquiring enough training data, the authors also successfully explore the use of a modified Cycle-GAN (General Adversarial Network) to produce synthetic thermal training data. The paper presents results using curves of the precision and recall of the detector and the authors conclude that the thermal detector achieves better performance than the visible one, both in real and synthetic data. Sadly any details on the distance between the sensor and the target drone is omitted. Finally, the authors claim that the visible and thermal datasets used are made available as the “USC drone detection and tracking dataset”, without giving any link in the paper. This dataset is also mentioned in [18], but the link found in that paper is unfortunately not working. Compared to the results of [17], as summarized above, the present

paper will make use of three different drone types instead of just one in the data set. It will also expand the number of target classes of the detector to four and additionally explore the detection performance as a function of sensor-to-target distance.

A thermal infrared camera is also used as one of the sensors in [9], but just as pointed out in [5], this paper, like several others, fails to specify the type, field of view or even the resolution of the used sensors, so even if there are useful tables of the results, any comparison is unfortunately hard to achieve.

2.2. Sensors in the Visible Range

A widespread method to detect drones, as described in recent scientific papers, is to combine a video camera with a detector based on a convolutional neural network (CNN). One of these papers [19], published in 2017, makes an in-depth study of the performance of six different CNN-models. The paper presents metrics for training time and performance in speed (frames per second) as well as curves for precision and recall. After comparing the six different solutions, the authors conclude that, considering speed and accuracy trade-offs, YOLOv2 [20] seems to be the most appropriate detection model.

As it turns out, when studying the subject of drone detection in images in the visible range, the YOLOv2-architecture is very common. In [18], [21], [11] and [12], this is the preferred and implemented CNN-model. A lightweight version of the more recent YOLOv3 is utilized in [22]. The success of the YOLOv2 motivates its use in the present paper. This choice will also make it possible to compare the results to the papers mentioned above.

The fact that the two primary sensors (IR and visible) of the drone detector system in the present paper are placed on a pan/tilt platform also arises the need for a wide-angle sensor to steer the sensors in directions where suspicious objects appear. In [22], a static camera with 110° field of view (FoV) is used to align a rotating narrow-field camera, whose images are analysed with the YOLOv3-model as pointed out above. To find the objects to be investigated further by the narrow-field camera, the video stream from the wide-angle one is analysed by means of a Gaussian Mixture Model (GMM) foreground detector [23]. A GMM foreground detector will also be implemented in the present paper for the wide-angle sensor. However, the one that we will use has an even wider FoV (180°). Just as pointed out in [22], this setup is prone to produce false alarms in some situations, but as described later, this can be mitigated by tuning the associated detection and tracking algorithms.

Of all papers found using versions of the YOLO architecture for drone detection, [21] has the most output target classes with three (drone, airplane and helicopter), followed by [12] with two classes (drone and bird). However, none of the YOLO papers report the detection accuracy as a function of the sensor-to-target distance.

2.3. Acoustic Sensors

Numerous papers have also explored the possibility to detect drones using acoustic sensors. Some of these papers, like [24], [25] and [26] utilize the Fast Fourier Transform (FFT) to extract features from the audio signals. However, it is observed that the Mel Frequency Cepstrum Coefficients (MFCC) seems to be the most common feature extraction technique, as used in [27], [28], [29] and [30]. The MFCC consists of a non-linear mapping of the original frequency according to the auditory mechanism of the human ear, and it is the most commonly used audio feature in current drone recognition tasks [21].

When comparing classification models for the drone detection task, the authors of [29] comes to the conclusion that Long Short-Term Memory (LSTM) [31] achieves the best performance and F1-score. In that paper, the classification is binary (drone or background). The present work expands the range of output classes of [29] by adding a helicopter class.

Also, the maximum acoustic detection range reported in the reviewed papers is 290 m [32], using a 120-element microphone array and a DJI Phantom 2 drone. It is worth noting that the the DJI Flame Wheel F450, one of the drones used in this work, is detected at distance of 160 m by the microphone array.

2.4. Radar

Since radar is the most common technology to detect flying objects, it is not far fetched to apply this also to the detection of drones. Doing this with a radar system designed to detect aircrafts is however not as straight forward as it might seem, since those systems often have features to reduce unwanted echoes from small, slow and low-flying objects, which is precisely what characterise the drones in question.

The small Radar Cross Sections (RCS) of medium-sized consumer drones are well described in [33], and from [34] we have that the RCS of the DJI Flame Wheel F450 is -17 dBsm (0.02 m^2). The results of [35] point out that flying birds have similar RCS, something that can lead to false targets when detecting drones. The F450 drone is also used in [36], where the micro-doppler characteristics of drones are investigated. These are typically echoes from the moving blades of the propellers and can be detected on top of the bulk motion doppler signal of the drone. Since the propellers are generally made from plastic materials, the RCS of these parts are even smaller and in [33], it is stated that the echoes from the propellers are 20 to 25 dB weaker than that of the drone body itself. Nevertheless, papers like [37], [38] and [39] accompany [36] in exploring the possibility to classify drones using the micro-doppler signature.

2.5. Other Drone Detection Techniques

Very few drones are autonomous in the flight phase. Generally, they are controlled by a manned ground equipment, and often the drones themselves also send out information on some radio frequency (RF), which can be used to detect them as well. The three drones used in this work are all controlled in real-time. The information sent out by the drones can range from just simple telemetry data such as battery level (DJI Flame wheel F450), a live video stream (Hubsan H107D+), to both a video stream and extensive position and status information (DJI Phantom 4 Pro). Utilizing the RF fingerprint is described in [40], and in [41], a CNN is used to process the information from an antenna array so that the direction to the drone controller can be calculated within a few degrees. In [42], signals from 15 different drone controllers are classified with an accuracy of 98.13% using only three RF features (shape factor, kurtosis and variance) with a K-Nearest Neighbour (KNN) classifier. The use of LiDAR (Light Detection And Ranging) and LADAR (LAsER Detection And Ranging) has been also explored [43], successfully detecting drones up to a distance of 2 km.

2.6. Sensor Fusion

The paper [8] mentioned fusion of data from multiple sensors as a way to improve accuracy, since sensor combination helps in compensating weaknesses of the individual sensors. As mentioned above, the benefits of sensor fusion are also pointed out in [7]. Considering that missed detection of an intruding drone will bring more security threats than false alarms, the authors of [10] conduct audio, video and RF detection in parallel, using a logical OR operation to fuse the results of the three detectors. They also highlight that combination of such heterogeneous data sources is an open research question, since the simple combination of the results separately obtained by audio, video, and RF surveillance can induce great information loss. In contrast, it would be of greater significance to develop reliable fusion techniques at the feature level as well. Without any further specifications of the sensors used besides that they are visible, thermal and 2D-radar, the work [9] presents promising results from experiments

using a multilayer perceptron (MLP) to perform sensor fusion in a drone detector/classifier with just one output class. Just as in [8], the present paper also considers early and late sensor fusion and differentiate these two principles based on if the sensor data is fused before or after the detection element.

2.7. Drone Detection Datasets

As mentioned, the work [5] points out the lack of a publicly available datasets. This is also the case in [8], where the authors highlight this especially in the case of thermal infrared cameras. They conclude that creating a dataset for UAV detection with thermal images might be budget-wise out of reach of many universities and research centers. They also state the strong need of real-world UAV audio datasets that could serve as research benchmarks.

In the references of [8], there are two useful links to datasets for visible video detectors. One of these is [44], where 500 annotated drone images can be found. This is far away from the 203k images of our database (plus audio clips). The other link leads to the dataset [45] of the drone-vs-bird challenge held by the Horizon2020 SafeShore project consortium. However, the dataset is only available upon request and with restrictions to the usage and sharing of the data. The drone-vs-bird challenge is also mentioned in [11], [12] and by the winning team of the challenge in 2017 [46].

The dataset used in [22] is not publicly available due to confidentiality. Since the work of that paper was funded by the French Ministry of Defence, one can presume that the dataset, in one way or another, is a property of the French Government or the French Armed Forces.

3. Materials and Methods

This section describes the proposed methodology and outlines the automatic drone detection system, first on a system-level and then, in deeper detail. We detail the hardware components, how they are connected to the main computational resource, and the involved software running in the drone detection system, including the graphical user interface. The methods used for the composition of our dataset are also described, including a description of the dataset, its division per sensor type, target class and sensor-to-target distance. Our descriptive approach is motivated by [5], which highlights that most works on visual drone detection do not specify the acquisition device, drone type, detection range, or dataset, all being key details that allow replication and comparison with other works.

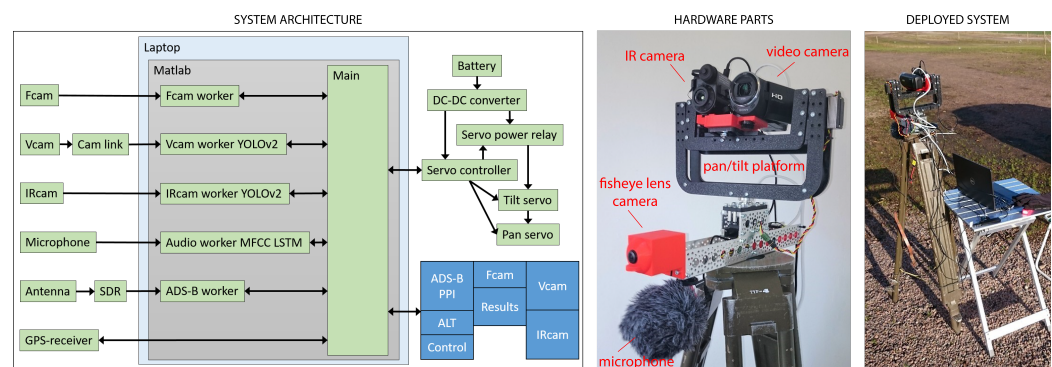


Figure 1. Left: system architecture with hardware and software parts. Center: main hardware parts of the detection system. Right: the system deployed just north of the runway at Halmstad airport (IATA/ICAO code: HAD/ESMT). Pictures originally appearing in [47] and published in [13]. Reprinted with permission.

3.1. Architecture of the System

A drone detection system must be able to both cover a large volume of airspace and have sufficient resolution to distinguish small objects like drones, and tell them apart from another types of objects. Combining wide and narrow field of view (FoV) cameras is one way to accomplish this [22]. Another way, shown in [21], is to use an array of high-resolution cameras. Here, we follow the first approach, since our solution has been designed with portability in mind (Figure 1, right). Since the present paper uses only one infrared sensor with a fixed FoV, there is no possibility to have neither a wide-angle infrared sensor or an array of such sensors. The proposed way to achieve the desired volume coverage with the IR-sensor is to have it on a moving platform, as shown in Figure 1, center. This platform can then either have objects assigned to it or search by itself at moments in time when the sensors are not busy detecting and classifying objects. The overall system architecture, detailing the hardware and software components employed, is shown in Figure 1, left. The layout of the components of the Graphical User Interface (GUI) is shown in the bottom right part (boxes in blue).

To be able to react to moving objects and also to have the ability to track those, the combined time-constraints of the detection cycle and the control loop of the moving platform means that the system must work in close to real-time. Hence, all the detection and classification processes must be done efficiently and with as little delay as possible. The feedback loop of the moving platform must run at sub-second speed. To be able to put together such a system, involving both several sensors and mechanical parts, makes the importance of choosing the right methods critical. All these constraints, in turn, imposes demands on the efficiency of the software as well. Another aspect is that to detect the drones with high efficiency, the system must also recognize and track other flying objects that are likely to be mistaken for a drone. For some of these drone-like objects, this is indigenous hard, e.g. birds. For others, it is technically possible since some of them announce their presence and location via radio, e.g. ADS-B, over which most aircrafts regularly transmit messages with varied content. Combining the data from several sensors under the time constraints described above must be kept simple and streamlined too. This, together with the fact that very few papers have explored sensor fusion techniques, is the motivation to have a system where the inclusion and weights of the sensors can be altered at runtime to find a feasible setting.

3.2. Hardware

As primary electro-optical sensors, we use a thermal infrared camera (denoted as IRcam in Figure 1, left) and a video camera (Vcam). Our system can keep track of cooperative aircrafts via ADS-B information that is made available with an antenna, which collects the aircraft's position, velocity vectors and identification information that is broadcasted by aircrafts equipped with such system. We also include audio information through a microphone, which is employed to distinguish drones from other objects in the vicinity such as helicopters. All computations are made in a standard laptop, which is also used to present the results to the user via the designed GUI.

Since the primary cameras have a limited FoV, a fish-eye lens camera (Fcam) covering 180° horizontally and 90° vertically is also used. The fish-eye camera is used to detect moving objects in its FoV and then, steer the IRcam and Vcam towards the detected objects using the pan/tilt platform. If nothing is detected by the Fcam, the platform can be set to move in two different search patterns to scan the sky. As additional sensors, our system also includes a GPS receiver. To provide stability to the system, the hardware components are mounted on a standard surveyors tripod. This solution also facilitates the deployment of the system outdoors, as shown in Figure 1, right. Due to the nature of the system, it must also easily be transported to and from any deployment. Hence, the system can be disassembled into a few large parts and placed in a transport box.

3.2.1. Thermal Infrared Camera (IRcam)

We employ a FLIR Breach PTQ-136 using the Boson 320×256 pixels detector (Y16 with 16-bit grey scale). The FoV of the IRcam is 24° horizontally and 19° vertically. It is worth noting that this sensor has a higher resolution compared to the FLIR Lepton sensor with 80×60 pixels that was used in [16]. In that paper, the authors detected three drone types up to a distance of 100m. However, it was done manually by a person looking at the live video stream. In contrast, the present paper employs an automatic detection solution. The signal of the IRcam is sent to the laptop at 60 frames per second (FPS) using the USB-C port, which also powers the IRcam.

3.2.2. Video Camera (Vcam)

To capture video in the visible range, we employ a Sony HDR-CX405 video camera. The feed is taken from the HDMI port, which is captured with an Elgato Cam Link 4K frame grabber that provides a 1280×720 video stream in YUY2-format (16 bits per pixel) at 50 FPS. The FoV of the Vcam can be made wider or narrower using its adjustable zoom lens. In this work, it is adjusted to have about the same FoV of the IRcam.

3.2.3. Fish-eye Lens Camera (Fcam)

To counteract the limited FoV of the IRcam and Vcam, a fish-eye lens camera is used to monitor a wider area of the sky, and then steer and focus these two towards the detected objects to ascertain if they are drones or something else. The fish-eye lens camera employed is a ELP 8 megapixel with a FoV of 180° degrees, which provides a 30FPS 1024×768 video stream in Mjpg-format at 30 FPS via USB.

3.2.4. Microphone

The microphone is used to distinguish drones from other objects emitting sounds, as for example helicopters. Here, we use a Boya BY-MM1 mini cardioid directional microphone, which is connected directly to the laptop.

3.2.5. ADS-B Receiver

To track aircraft equipped with transponders, an ADS-B receiver is also used. This consists of an antenna and a NooElec Nano 2+ Software Defined Radio receiver (SDR). This is tuned to 1090 MHz so that the identification and positional data sent out as a part of the 1 Hz squitter message can be decoded and displayed. The Nano 2+ SDR receiver is connected to the laptop via USB.

3.2.6. GPS receiver

To present the decoded ADS-B data in a correct way the system is also equipped with a G-STAR IV BU-353S4 GPS receiver connected via USB. The receiver outputs messages following the National Marine Electronics Association (NMEA) format standard.

3.2.7. Pan/tilt platform and servo controller

The pan/tilt platform is a Servocity DDT-560H direct drive tilt platform together with the DDP-125 Pan assembly, also from Servocity. To achieve the pan/tilt motion, two Hitec HS-7955TG servos are used. A Pololu Mini Maestro 12-Channel USB servo controller is included so that the respective position of the servos can be controlled from the laptop. Since the servos have shown a tendency to vibrate when holding the platform in specific directions, a third channel of the servo controller is also used to give the possibility to switch on and off the power to the servos using a small opto-isolated relay board.

To supply the servos with the necessary voltage and power, both a net adapter and a DC-DC converter are available. The DC-DC solution is used when the system is deployed



Figure 2. The data collection setup using a lighter version of the system.

outdoors and, for simplicity, it uses the same battery type as one of the available drones. Some other parts from Actobotics are also used in the mounting of the system and the following has been designed and 3D-printed: adapters for the IR, video and fish-eye lens cameras, a radar module mounting plate and a case for the servo controller and power relay boards.

A lighter version of the IRcam and Vcam mounting without the pan/tilt platform has also been prepared. This is used on a light camera tripod when collecting the dataset, and hence simplifies both transporting the setup and also the possibility for a person to manually set the direction of it. The data collection setup is shown in Figure 2.

An unforeseen problem occurring when designing the system was actually of mechanical nature. Even though the system uses a pan/tilt platform with ball-bearings and very high-end titanium gear digital servos, the platform was observed to oscillate in some situations. This phenomena was mitigated by carefully balancing the tilt platform and by introducing some friction in the pivot point of the pan segment. It might also be the case that such problems could be overcome using a servo programmer. Changing the internal settings of the servos could also increase their maximum ranges from 90° to 180° . This would extend the volume covered by the thermal infrared and video cameras, so that all targets tracked by the fish-eye camera could be investigated, not just a portion of them, as now.

3.2.8. Computer

The computational part of the system is handled by a Dell Latitude 5401 laptop. This is equipped with an Intel i7-9850H CPU and an Nvidia MX150 GPU. The laptop is connected to all of the above-mentioned sensors and the servo controller using the built-in ports and an additional USB-hub, as shown in Figure 1, right.

It is observed, regarding the sensors, that there is a lower limit of around 5 FPS where the system becomes so slow that the ability to track flying objects is lost. All actions taken by the system have to be well balanced, and just such a simple thing as plotting the ADS-B panel with a higher frequency than necessary can cause a drop in the FPS rate. Such problems can be overcome by the use of more than one computational resource.

3.2.9. Radar module

As indicated earlier, our solution does not include a radar module in its final deployment. However, since one was available, it was included in our preliminary tests. It is a radar module from K-MD2, whose specifications are shown in Figure 3 [48]. Its exclusion was motivated by its short practical detection range. Interestingly, the K-MD2 radar module is also found to be used in another research project connected to drones [49], not to detect drones, but instead mounted on board one as part of the navigation aids in GNSS2 denied environments.

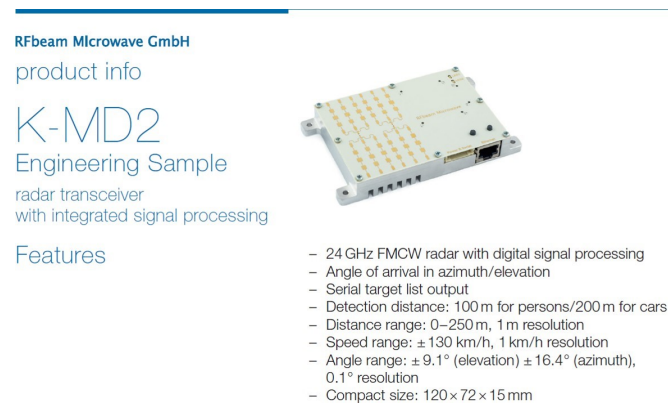


Figure 3. The radar module K-MD2.

3.3. Software

Matlab is the primary development environment on which the drone detection system has been developed. The software for drone detection consists of a main script and five separate ‘workers’, one per sensor, as shown in Figure 1, left. The main script and the workers can run asynchronously and in parallel, enabled by the Matlab parallel computing toolbox. This allows each detector to run independently of the others, This also allows the different detectors to run asynchronously, handling as many frames per second as possible without any inter-sensor delays and waiting time. The main script communicates with the workers using pollable data queues. The *Fcam worker* utilizes a foreground/background detector via GMM background subtraction [23], together with a multi-object Kalman filter tracker. After calculating the position of the best-tracked target (defined as the one with the longest track history), it sends the azimuth and elevation angles to the main script, which then controls the pan/tilt platform, so that the moving object can be analysed further by the IR and video cameras. The *IRcam* and *Vcam* workers are similar in their basic structure and both import and run a trained YOLOv2 detector, fine-tuned with annotated ground truth to work with data from each camera. The information sent to the main script is the region of the image where the object has been detected, the class of the detected target found in the ground truth of the

training dataset, the confidence, and the horizontal and vertical offsets in degrees from the centre point of the image. The latter is used to calculate servo commands and track the object. The *Audio* worker sends information about the class and confidence to the main script. It uses a classification function built on an LSTM-architecture, which is applied to MFCC features extracted from audio signals captured with the microphone. Unlike the others, the *ADS-B* worker has two output queues, one consisting of current tracks and the other of the history tracks. This is done so that the presentation clearly shows the heading and altitude changes of the targets. All of the above workers also send a confirmation of the command from the main script to run the detector/classifier or to be idle. The number of frames per second currently processed is also sent to the main script.

Table 1 shows the different classes that each worker is able to provide to the main script. Note that not all sensors can output all the target classes. The audio worker has an additional “background” class, and the ADS-B will output a “no data” class if the vehicle category field of the received message is empty (since it is not a mandatory field of ADS-B messages).

Table 1. Output classes of the sensors and their corresponding class colours.

Worker					
IRcam	AIRPLANE	BIRD	DRONE	HELICOPTER	
Vcam	AIRPLANE	BIRD	DRONE	HELICOPTER	
Audio			DRONE	HELICOPTER	BACKGROUND
ADS-B	AIRPLANE		DRONE	HELICOPTER	NO DATA

3.3.1. Main Script

This is the core of the system. Besides starting the five workers (threads) and setting up the queues to communicate with these, it also sends commands to and reads data from the servo controller and the GPS-receiver. After the start-up sequence, the script goes into a loop that runs until the program is stopped by the user via the graphical user interface (GUI).

Updating the GUI and reading user inputs are the most frequent tasks on every iteration of the loop. At regular intervals, the main script also interacts with the workers and the servo controller. Servo positions are read and queues are polled ten times a second. The system results, i.e. the system output label and confidence, are also calculated using the most recent results from the workers. Furthermore, at a rate of 5 Hz, new commands are sent to the servo controller for execution. Every two seconds the ADS-B plot is updated. Having different intervals for various tasks makes the script more efficient since, for example, an aircraft sends out its position via ADS-B every second, and hence, updating the ADS-B plots too often would only be a waste of computational resources.

3.3.2. IRcam worker

Raw images are processed with Matlab function `imflatfield` for 2-D image flat-field correction (with $\sigma=30$) followed by `imadjust` to increase image contrast. Flat-field correction uses Gaussian smoothing to approximate the shading component of the input image. Next, the input image is processed by the YOLOv2-detector, with a given detection threshold and the execution environment set to GPU. The output from the detector consists of an array of class labels, confidence scores and bounding boxes for all objects that have been detected and classified. The detector output may be no data at all, or just as well, data for several detected objects. In this implementation, only the detection with the highest confidence score is sent to the main script. Images from the IR camera are of 320×256 pixels. To present the result in

the GUI at the same size than the Vcam output, the image is resized to 640×512 . Then, the bounding box together with the class label and confidence score are inserted in the image. To clearly indicate the detected class, the inserted annotation uses the same colour scheme as presented in Table 1. The current state of the detector and its performance (frames per second) is also inserted in the top left corner of the image, and such information is also sent to the main script together with the detection results.

The YOLOv2 detector employed is formed by modifying a pretrained MobileNetv2 following [50], so that the first 12 layers out of 53, are used for feature extraction. The input layer is updated so that it has the size of $256 \times 256 \times 3$. Six detection layers and three final layers are also added to the network. Besides setting the number of output classes of the final layers, the anchor boxes used are also specified. To estimate the numbers of anchor boxes to use and the size of these, the training data is processed using the `estimateAnchorBoxes` function. This function uses a *k*-means clustering algorithm to find suitable anchor boxes sizes given the number of boxes to be used. We test the number of anchor boxes from one to nine to provide a plot over the mean intersection over union (IoU) as a function of the number of boxes, as shown in Figure 4.

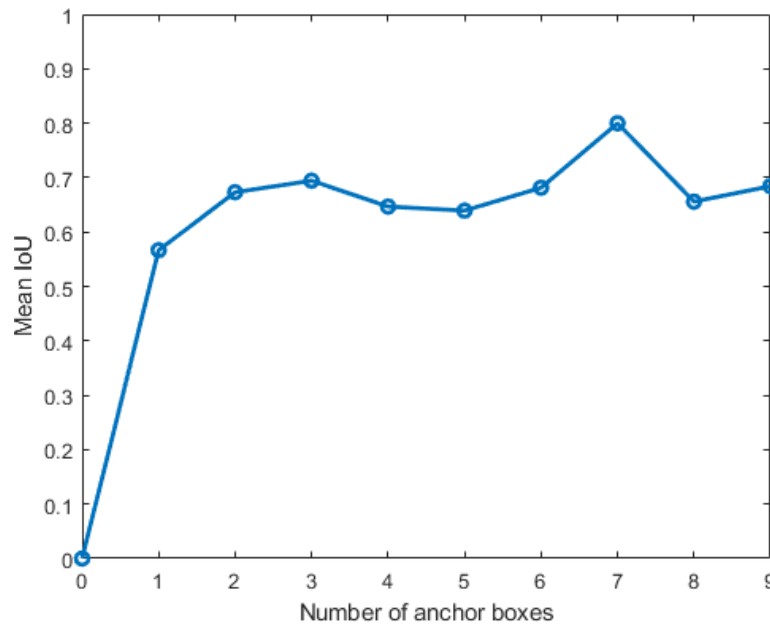


Figure 4. Plot used to assess the number of anchor boxes to be implemented in the IRcam worker YOLOv2 detector.

When choosing the number of anchor boxes to use, the trade-off to consider is that a high IoU ensures that the anchor boxes overlap well with the bounding boxes of the training data but, on the other hand, using more anchor boxes will also increase the computational cost and may lead to over-fitting. After assessing the plot, the number of anchor boxes is chosen to be three, and the sizes of these (with the scaling factor of 0.8 in width to match the downsize of the input layer from 320 to 256 pixels) are taken from the output of the `estimateAnchorBoxes` function.

The detector is trained with `trainYOLOv2ObjectDetector` using data picked from the available dataset (Section 4). The detector is trained for five epochs using the stochastic gradient descent with momentum (SGDM) optimizer and an initial learning rate of 0.001. Using a computer with an Nvidia GeForce RTX2070 8GB GPU, the time for one epoch is 39 min. The training function includes pre-processing augmentation consisting of horizontal flipping

(50% probability), scaling (zooming) by a factor randomly picked from a continuous uniform distribution in the range $[1, 1.1]$, and random color jittering for brightness, hue, saturation, and contrast.

3.3.3. Vcam worker

To be able to compare their results, the methods and settings of the Vcam worker are very similar to the IRcam worker above, with some exceptions. Images are of 1280×720 pixels, which are then resized to 640×512 without further pre-processing. Given the bigger image size, the input layer of the YOLOv2 detector here has a size of $416 \times 416 \times 3$. Due to the increased image size, the training time is also extended compared to the IR case. When using a computer with an Nvidia GeForce RTX2070 8GB GPU, the time for one epoch is 2 h 25 min. The detector is trained for five epochs, just as the IRcam detector.

3.3.4. Fcam worker

Initially, the fish-eye lens camera was mounted facing upwards, but this caused the image distortion to be significant in the area just above the horizon where the interesting targets usually appear. After turning the camera so that it faces forward (as can be seen in Figure 1, center), the motion detector is less affected by image distortion.

The images from the camera are of 1280×768 pixels, but the lower half (showing the area below the sky horizon) is cropped, so that 1024×384 pixels remain to be processed. Images are then analysed using the `ForegroundDetector` function. This uses a background subtraction algorithm based on Gaussian Mixture Models (GMM). The output from this function is a binary mask where pixels of moving objects set to one. The mask is next processed with the `imopen` function that performs a morphological erosion followed by a dilation. The structural element is set to 3×3 so that very small objects are deleted. Then, the `BlobAnalysis` function is applied, which outputs an array of centroids and bounding boxes for all objects that are considered to be moving. All centroids and bounding boxes are sent finally to a Kalman filter multi-object tracker [51]. The object with the longest track history is picked out and retained as the best one.

In the Fcam presentation window, all tracks (both updated and predicted) are visualised, and the track considered to be the best is marked with red colour (Figure 5). The output from the Fcam worker is the FPS-status, together with the elevation and azimuth angles of the best track, if such track exists at the moment. Of all the workers, the Fcam is the one with most tuning parameters, as will be seen in Section 4. This involves choosing and tuning the image processing operations, the foreground detector and blob analysis settings, and finally the multi-object Kalman filter tracker parameters.



Figure 5. Fish-eye camera image with a detected track in red.

3.3.5. Audio worker

The audio worker collects acoustic data in a one-second long buffer (44100 samples), set to be updated 20 times per second. To classify the source of the sound in the buffer, it is first processed with the `mfcc` function to extract MFCC features. Based on empirical trails, the parameter `LogEnergy` is set to `Ignore`, and then the extracted features are sent to the classifier. The LSTM-classifier used consists of an input layer, two bidirectional LSTM layers with a drop out layer in-between, a fully connected layer, followed by a softmax layer and a classification layer. The classifier builds on [52] but increasing the number of classes from two to three, and an additional dropout layer between the bidirectional LSTM layers.

The classifier is trained from scratch for 120 epochs, after which it starts to show signs of over-fitting. It includes a class of general background sounds (Table 1) recorded outdoors in the typical deployment environment of the system, and also include some clips of the sounds from the servos moving the pan/tilt platform. Like the other workers, the output is a class label together with a confidence score. A graphical presentation of the audio input and extracted features is also available as shown in Figure 6, but this is not included in the final GUI-layout.

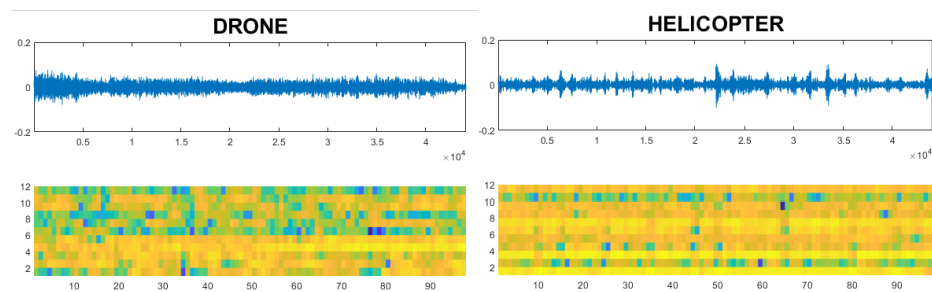


Figure 6. Two examples of the audio worker plots with the audio amplitudes and the extracted MFCC features.

3.3.6. ADS-B worker

We implement the ADS-B decoding in Matlab using functions from the Communications toolbox [53]. All vehicle categories that can be seen as subclasses to the airplane target label are clustered together. These are all the classes “Light”, “Medium”, “Heavy”, “HighVortex”, “VeryHeavy” and “HighPerformanceHighSpeed”. The class “Rotocraft” is translated into helicopter. Interestingly, there is also a “UAV” category label. This is also implemented in the ADS-B worker, translated into drone.

One might wonder if there are any such aircraft sending out that they belong to the UAV vehicle category. Examples are in fact found looking at the Flightradar24 service (Figure 7). Here we can find one such drone flying at Gothenburg City Airport (left), one of the locations used when collecting the dataset. The drone is operated by the company Everdrone AB, involved in the automated external defibrillators delivery trails of [54]. Another example is the UK Coastguard/Border Force surveillance drone that is regularly flying at night over the straight of Dover since December of 2019. This is naturally a large drone with a wingspan of 7.3 m.

As mentioned above, not all aircrafts will send out their vehicle category as part of the ADS-B squitter message. However, in our experience, about half of the aircrafts send out their category. This justifies its inclusion in this work, as one of our principles is to detect and keep track of other flying objects that are likely to be mistaken by a drone. In the output message of the ADS-B worker, the confidence of the classification is set to 1 if the vehicle category message has been received. If not, the label is set to airplane (the most common aircraft type) with the

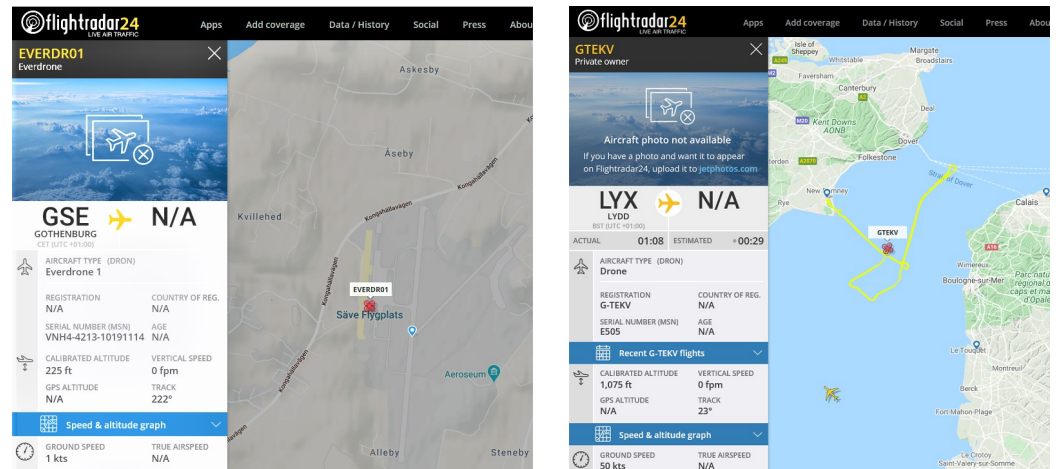


Figure 7. Left: A drone flying at Gothenburg City Airport. Right: Surveillance drone over the strait of Dover. Images from www.flightradar24.com

confidence to 0.75, so that there is a possibility for any of the other sensors to influence the final classification.

3.4. Graphical User Interface (GUI)

The Graphical User Interface of the system is shown in Figure 8. The GUI is part of the main script, but it is described separately. It shows the output of the different workers, including video streams of the cameras, providing as well different options to control the system configuration. The Matlab command windows is made visible in the bottom center part, so that messages (e.g. exceptions), can be monitored during the development and use of the system.

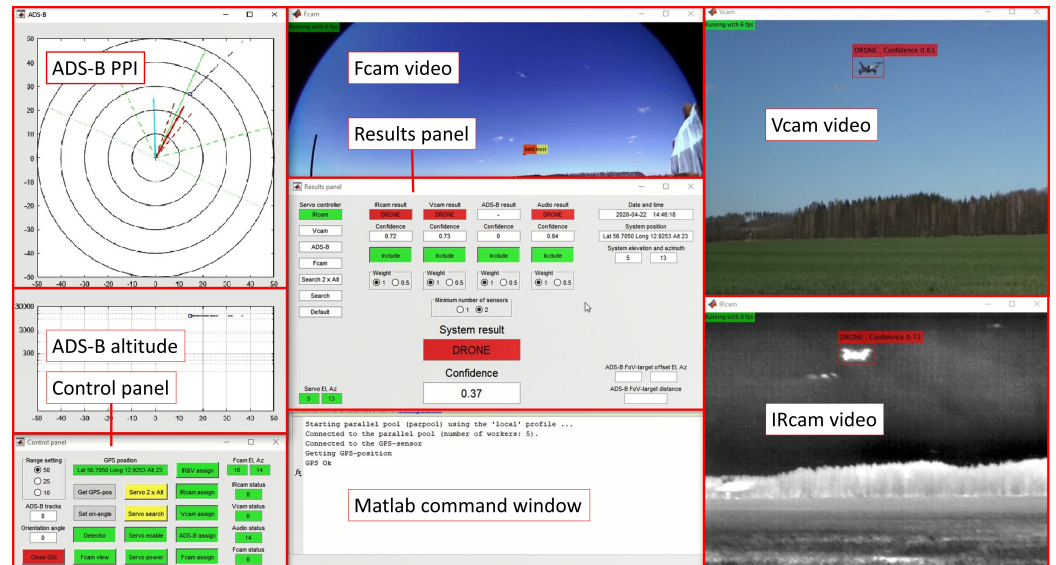


Figure 8. Graphical User Interface of the system with labels of the different elements. Picture originally appearing in [47] and published in [13]. Reprinted with permission.

The ADS-B presentation area (left) consists of a PPI-type (Plan Position Indicator) display and an altitude display. Besides presenting the ADS-B targets, the PPI display is also used to

present system information. The solid green line is the main direction of the system relative to the north. The other green lines present the field of motion of the pan/tilt platform (dashed) and the field of view of the fish-eye lens camera (dotted). The actual direction of the pan/tilt platform is presented with a solid red line and the field of view of the thermal infrared and video cameras are represented using dashed red lines. If any object is tracked by the fish-eye lens camera worker, its direction is indicated by a solid cyan line. ADS-B targets are presented using the class label colours of Table 1, together with the track history plots. The presentation of the altitude information is done in a logarithmic plot so that the lower altitude portion is more prominent.

The area directly below the ADS-B presentation is the control panel (seen in better detail in Figure 9, left). Starting from the top left corner, we have radio-buttons for the range settings of the ADS-B PPI and altitude presentations. Next, it is the number of ADS-B targets currently received and below that, the set orientation angle relative to the north. The “Close GUI” button is used to shut down the main script and the workers. The GPS-position presentation changes colour to green when a valid position has been received from the GPS-receiver, after pressing the “Get GPS-pos” button. A press on the “Set ori-angle” button opens an input dialogue box, so that the orientation angle of the system can be entered. Below that two buttons for switching the detectors between running and idle mode, and a choice to display the raw Fcam image or the moving object mask only (not shown). The servo settings can be controlled with the buttons of the mid column. To aid the Fcam in finding interesting object, the pan/tilt can be set to move in two different search patterns. One where the search is done from side to side using a static elevation of 10° , so that the area from the horizon up to 20° is covered, and another one where the search is done with two elevation angles to increase the coverage. The pan/tilt platform can also be controlled by the elevation and azimuth angles from one of the workers. This is set by the “assign” buttons of the fourth column, placed in priority order from top to down. The “IR&V assign” setting means that a target has to be detected by both of the IRcam and Vcam workers, and if so, the pan/tilt platform is controlled by the angular values from the IRcam worker. The rightmost column of the control panel shows the status information regarding the performance in FPS of the workers, and the elevation and azimuth angles of the Fcam worker target (if such target exists). The status displays are red if the worker is not connected, yellow if the detector is idle, and green if it is running.

The results panel (seen in better detail in Figure 9, right) features settings for the sensor fusion and presents the workers and system results. The first column (servo controller) indicates the source of information currently controlling the servos of the pan/tilt platform. In the bottom left corner, the angles of the servos are presented. The settings for the sensor fusion and the detection results presentation are found in the middle of the panel. The information in the right part of the panel is the current time and the position of the system. The system elevation and azimuth relative to the north are also presented here. Note the difference in azimuth angle compared to the bottom left corner where the system internal angle of the pan/tilt platform is presented. The last part of the results panel (bottom right corner) presents offset angles for the ADS-B target, if one is present at the moment in the field of view of the thermal infrared and video cameras. These values are used to detect systematic errors in the orientation of the system. The sloping distance to the ADS-B target is also presented.

3.5. Database

To accomplish the necessary training of the detectors and classifiers, a dataset has been also collected. The annotation has been done so that the dataset can be inspected, edited and used by others. The fact that the datasets for the thermal infrared and the visible video sensors are collected under the same conditions and using the same targets ensures that a comparison between the two sensor types is well-founded. The dataset is fully described

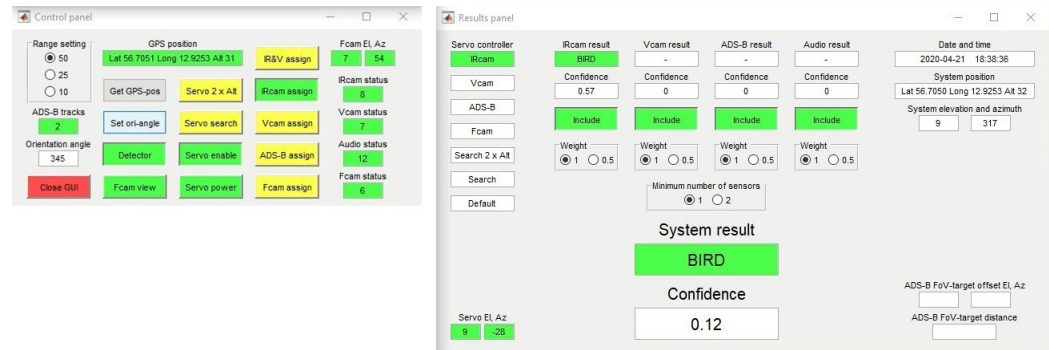


Figure 9. Detail of the control panel (left) and results panel (right) of the Graphical User Interface. In the control panel, note a bird that is detected and tracked by the IRcam worker.

in [55] and available at [56]. The videos and audios are recorded at locations in and around Halmstad Airport (IATA/ICAO code: HAD/ESMT), Gothenburg City Airport (GSE/ESGP) and Malmö Airport (MMX/ESMS). Three different drones are used to collect and compose the dataset. These are of the following types: Hubsan H107D+, a small-sized first-person-view (FPV) drone; the high-performance DJI Phantom 4 Pro; and finally, the medium-sized kit drone DJI Flame Wheel. This can be built both as a quadcopter (F450) or in a hexacopter configuration (F550). The version used in this work is an F450 quadcopter. All three types can be seen in Figure 10. These drones differ a bit in size, with Hubsan H107D+ being the smallest having a side length from motor-to-motor of 0.1 m. The Phantom 4 Pro and the DJI Flame Wheel F450 are a bit larger with 0.3 and 0.4 m motor-to-motor side length, respectively. To comply with regulations (drones must be flown within visual range), the dataset is recorded in daylight, even if the thermal infrared or acoustic sensors could be effective even at night.



Figure 10. The three drones of our dataset. Left: Hubsan H107D+. Middle: DJI Phantom 4 Pro. Right: DJI Flame Wheel F450. Pictures originally appearing in [47] and published in [13] and [55]. Reprinted with permission.

To facilitate annotation, the videos and audio files are cut into ten-second segments. Acquisition was performed during the drastic reduction in air traffic due to the COVID19 pandemic. Therefore, to get a more comprehensive dataset, both in terms of aircraft types and sensor-to-target distances, the data is complemented with non-copyrighted material of [57]. Overall, the dataset contains 90 audio clips and 650 videos (365 IR and 285 visible, of ten seconds each), with a total of 203328 annotated images (publicly available). The thermal infrared videos have a resolution of 320×256 pixels, and the visible videos have 640×512 . The greatest sensor-to-target distance for a drone in the dataset is 200 m. Audio files consist of 30 ten-second clips of each of the three output audio classes (Table 1), and the amount of videos among the four output video classes is shown in Table 2. The background sound class contains general background sounds recorded outdoor in the typical deployment environment

of the system, and also includes some clips of the sounds from the servos moving the pan/tilt platform.

Table 2. Distribution of the thermal infrared and visible videos. Each video is has approximately 10 seconds. Reprinted with permission from [13].

bin	thermal infrared (365)				visible (285)			
	airpl.	bird	drone	helicopt.	airpl.	bird	drone	helicopt.
Close	9	10	24	15	17	10	21	27
Medium	25	23	94	20	17	21	68	24
Distant	40	46	39	20	25	20	25	10

The video part of the database is divided into three category bins: Close, Medium and Distant. This is because one of our aims is to explore performance as a function of the sensor-to-target distance. The borders between these bins are chosen to follow the industry-standard Detect, Recognize and Identify (DRI) requirements [58], building on the Johnson criteria [59], as shown in Figure 11. The Close bin is from 0 m to a distance where the target is 15 pixels wide (requirement for ‘identification’, e.g. explicitly telling the specific drone model, aircraft, helicopter, bird, etc.). The Medium bin is from where the target is from 15 down to 5 pixels (‘recognition’ of the target, e.g. a drone, an aircraft, an helicopter... albeit without the possibility of identifying the model), and the Distant bin is beyond that (‘detection’, e.g. there is something).

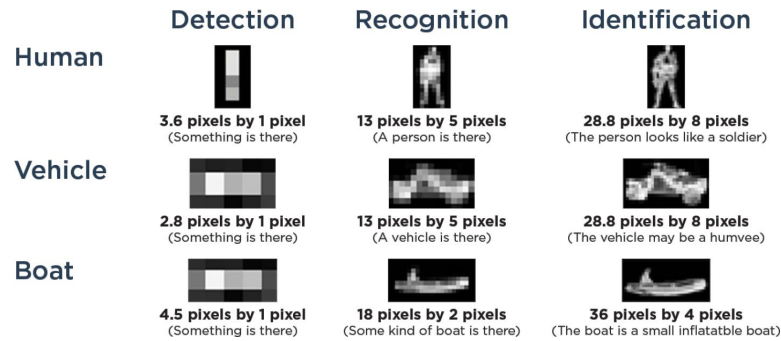


Figure 11. The DRI requirements (from [58]).

4. Results

We provide evaluation results of the individual sensors in terms of precision, recall and F1-score. Precision is the fraction of the total number of detections that are true positive, in other words, it measures how many of the detected objects are relevant. Recall is the fraction of the total number of labeled samples in positive class that are true positive, in other words, how many of the relevant objects are detected. With the video detectors, these metrics can be obtained using the function `bbboxPrecisionRecall`. Since we also have confidence scores, the `evaluateDetectionPrecision` function can be utilized to get plotted curves of precision as a function of the recall value. Thereafter, we carry out sensor fusion experiments as well, a direction barely followed in the related literature [9,10,22]. To carry out experiments, two disjoint sets of videos were created for training and testing (i.e. a video selected for the training set is not used in the testing set). The training set is composed of 120 infrared and 120 visible clips (10 for each class and target bin per spectrum), resulting in 37428 infrared frames and 37519 visible frames. The evaluation set is composed of 60 infrared and 60 visible clips (5

Table 3. Results with the thermal infrared sensor (confidence threshold and IoU requirement of 0.5). The average of the three F1-scores is 0.7601. Reprinted with permission from [13].

distance bin: CLOSE					
	airplane	bird	drone	helicopter	average
Precision	0.9197	0.7591	0.9159	0.9993	0.8985
Recall	0.87367	0.85087	0.87907	0.87927	0.8706
F1-score	0.88447				
distance bin: MEDIUM					
	airplane	bird	drone	helicopter	average
Precision	0.82817	0.50637	0.89517	0.95547	0.7962
Recall	0.70397	0.70337	0.80347	0.83557	0.7615
F1-score	0.77857				
distance bin: DISTANT					
	airplane	bird	drone	helicopter	average
Precision	0.78227	0.61617	0.82787	0.79827	0.7561
Recall	0.40437	0.74317	0.48367	0.45647	0.5218
F1-score	0.61757				

Table 4. Results with the thermal infrared sensor (confidence threshold 0.8, IoU requirement 0.5).

	distance bin			Average
	close	medium	distant	
Precision	0.9985	0.9981	1.0000	0.9987
Recall	0.2233	0.1120	0.0019	0.1124

for each class and target bin per spectrum), resulting in 18691 infrared frames and 18773 visible frames. Since the duration of each clip is roughly the same (~ 10 seconds), the amount of samples per class and target bin is approximately balanced. For the audio classifier, five 10-second clips from each output category are selected for evaluation, and the remaining clips for training. Since the audio classifier processes a one-second input buffer, the clips cut into that length, with overlap of 0.5 seconds. resulting in 20 samples per clip. This results in a total of 297 clips in the evaluation set, 99 from each class.

In evaluating the YOLOv2 detector, it provides an array of class labels, detection confidence, and bounding boxes of detected objects. Here, not only the classification label but also the placement of the bounding box must be taken under consideration. When it produces multiple bounding boxes for the same object, only the strongest one is used, chosen as the box with the highest IoU (Intersection Over Union) with the annotations in the training data. To assign a box to a class, it must also have a minimum IoU with the training object that it is supposed to detect. In related works, an IoU of 0.5 is usually employed [11,12,19], although a lower IoU of 0.2 is used in [46]. In this work, we will stick to 0.5. A threshold to the detection confidence can be also imposed, so bounding boxes with small confidence can be rejected, even if their IoU is above 0.5.

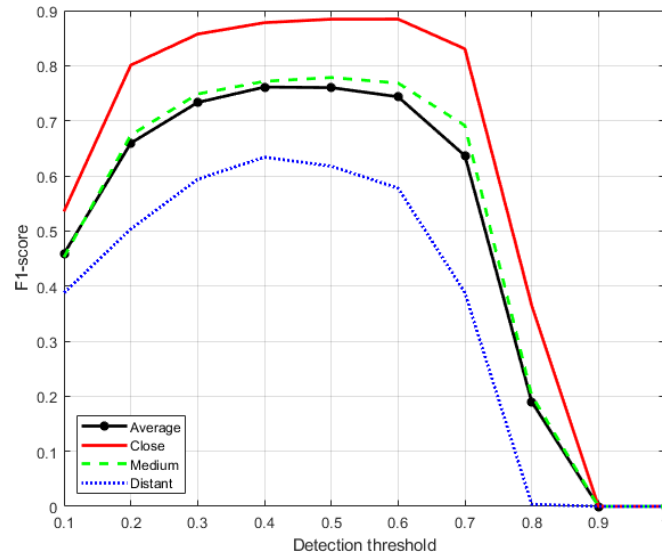


Figure 12. F1-score with the thermal infrared sensor as a function of detection threshold, using all the 18691 images in the evaluation dataset.

4.1. Thermal Infrared Camera (IRcam)

The precision, recall and F1-score of the IRcam worker detector with a confidence threshold set to 0.5 and an IoU requirement of 0.5 are shown in Table 3. We can observe that the precision and recall values are well balanced. Altering the setting to a higher decision threshold of 0.8 leads to higher precision, at the cost of a lower recall value, as shown in Table 4. The drop in recall with increasing sensor-to-target distance is also prominent.

To further explore the detection threshold setting, we run the evaluation with values from 0.1 up to 1.0 in steps of 0.1. The results in the form of F1-score are shown in Figure 12. Using not only the bounding boxes and class labels, but also the confidence scores, the detector can be evaluated in the form of precision vs. recall curves as well (Figure 13). Note that the average precision results output from the Matlab `evaluateDetectionPrecision` function is defined as the area under the precision vs. recall curve, hence it is not the same as the actual average precision values of Table 3. To distinct that we mean the area under the curve, we denote this as AP in Figure 13, just as in the original YOLO paper [20]. This is also the definition used in [11], and to further adopt the notation of these papers we denote the mean AP taken over all classes as the mAP, which is given in Table 5.

Table 5. Mean values over all classes of the area under the precision vs. recall curve (mAP) of the thermal infrared sensor.

	distance bin			Average
	close	medium	distant	
mAP	0.8704	0.7150	0.5086	0.7097

The choice of the detection threshold will affect the achieved precision and recall values. The stars in Figure 13 indicate the results with a detection threshold of 0.5 (as reported in Table 3). We can conclude that such threshold results in a balanced precision-recall combination near the top right edge of the respective curves. Compare this balanced behaviour to the precision and recall values obtained with a detection threshold of 0.8 (Table 4). From observations of the behaviour when running the drone detection system, we can also point out that a common

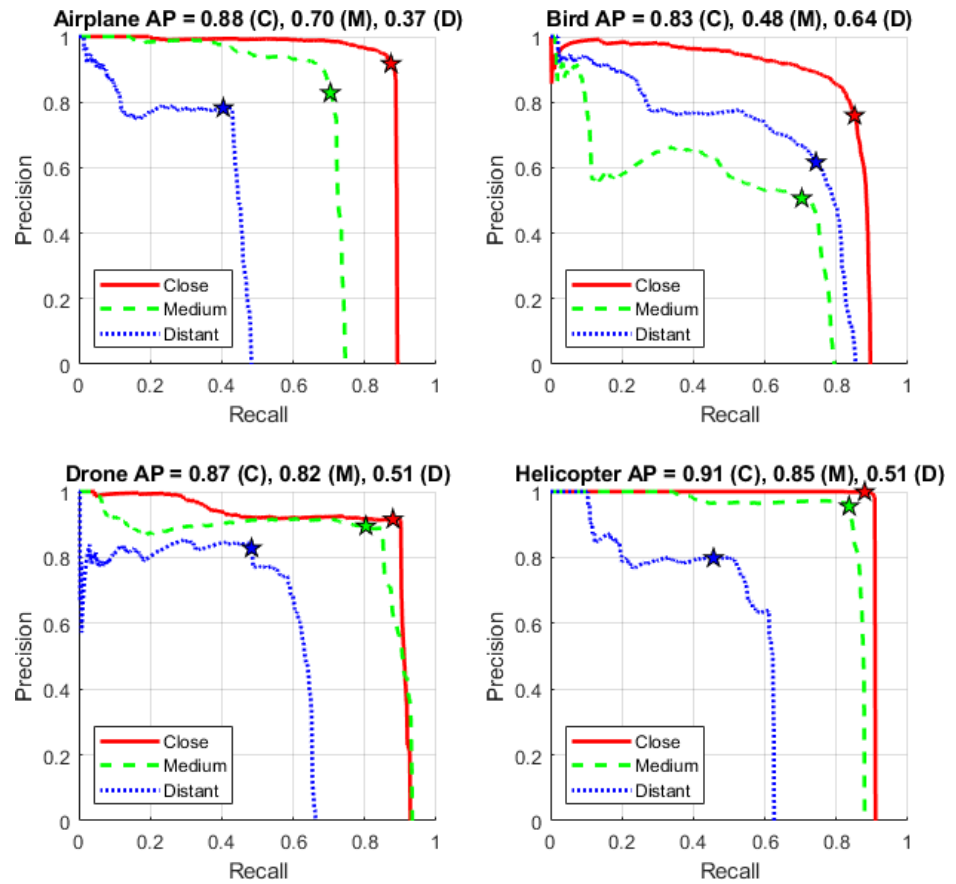


Figure 13. Precision and recall curves with the thermal infrared sensor. The achieved values with a detection threshold of 0.5 are marked by stars.

source of false alarms of the thermal infrared sensor are small clouds and edges of large clouds lit up by the sun. An example of this can be seen in Figure 14.

In comparing our work with other research making use of thermal infrared sensors, results can be found in [16]. However, the sensor used in that article to detect drones (up to a distance of 100 m) has a resolution of just 80×60 pixels, and the system does not involve any form of machine learning feature (the task is done by a human looking at the output video stream). In [17], curves for the precision and recall of a machine learning based thermal detector are presented. It is stated that the video clips used for training and evaluation have a frame resolution of 1920×1080 . Unfortunately, the paper fails to mention if this is also the resolution of the sensor. Neither is the input size if the detection network specified in detail, other than that the images are re-scaled so that the shorter side has 600 pixels. The most substantial results to relate to in [17] is that since the system also contains a video camera with the same image size as the thermal one, the authors can conclude that the thermal drone detector has a performance over 8% better than the video detector.

4.2. Video Camera (Vcam)

The results of the previous sub-section will be compared to the results of the video detector in what follows next. To enable comparison, the same methods and settings as the infrared camera are used here, leading to the precision, recall and F1-score results of Table 6 with a confidence threshold and IoU requirement of 0.5. These results differ no more than 3% from the results of the thermal infrared detector. Recall that the input layers of the YOLOv2 detectors



Figure 14. A false target of the thermal infrared sensor caused by a small cloud lit by the sun.

are different, and hence, the resolution of the visible detector is 1.625 higher than the thermal infrared detector (416×416 vs 256×256). So even with a lower resolution, and using images in grey-scale and not in colour, the thermal infrared sensor performs as well as the visible one. This is in line with [16], where the infrared detector outperforms the visible one when the image size is the same, although in our case this happens even with a smaller image size.

Table 6. Results with the visible camera (confidence threshold and IoU requirement of 0.5). The average of the three F1-scores is 0.7849. Reprinted with permission from [13].

distance bin: CLOSE					
	airplane	bird	drone	helicopter	average
Precision	0.8989	0.8284	0.8283	0.9225	0.8695
Recall	0.7355	0.7949	0.9536	0.9832	0.8668
F1-score					0.8682

distance bin: MEDIUM					
	airplane	bird	drone	helicopter	average
Precision	0.8391	0.7186	0.7710	0.9680	0.8242
Recall	0.7306	0.7830	0.7987	0.7526	0.7662
F1-score					0.7942

distance bin: DISTANT					
	airplane	bird	drone	helicopter	average
Precision	0.7726	0.6479	0.8378	0.6631	0.7303
Recall	0.7785	0.7841	0.5519	0.5171	0.6579
F1-score					0.6922

Just as for the thermal infrared camera, we can also explore the effects of the detection threshold setting. This can be seen in Figure 15. The precision vs recall curves of the video camera images for the different target classes and distance bins are shown in Figure 16. In a similar vein, a detection threshold of 0.5 results in a balanced precision-recall combination near the top right edge of the respective curves. Notably, when inspecting the precision-recall curves, the video camera detector performs outstandingly when it comes to distant airplanes. This has its explanation in that such targets often presents a very large signature consisting not only of the airplane itself but also contrails behind it. Also, calculating the mAP from these

results, we obtain Table 7, with an average of 0.7261. Once again, it is not far from the 0.7097 mAP of the thermal infrared detector of the previous sub-section.

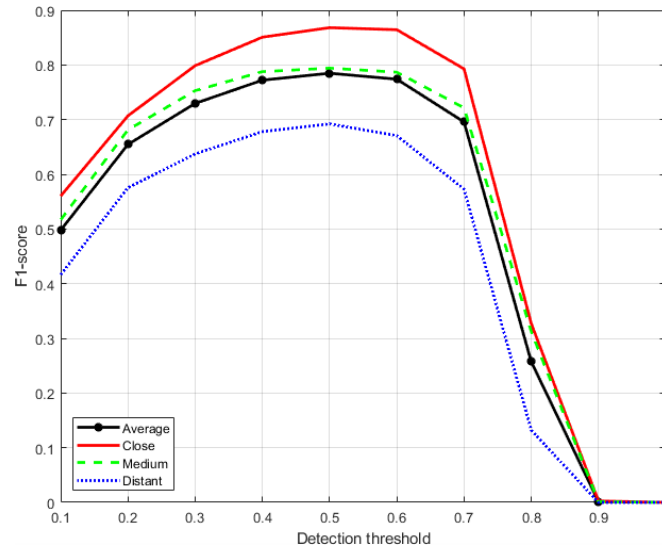


Figure 15. F1-score with the visible camera as a function of detection threshold, using all the 18773 images in the evaluation dataset.

Table 7. Mean values over all classes of the area under the precision vs. recall curve (mAP) of the visible camera.

	distance bin			Average
	close	medium	distant	
mAP	0.8474	0.7477	0.5883	0.7261

The most frequent problem of the video detector is the auto-focus feature of the video camera. For this type of sensor, clear skies are not the ideal weather, but rather a scenery with objects that can help the camera to set the focus correctly. However, note that this fact is not heavily affecting the evaluation results of the visible camera detector performance, as presented above, since only videos where the objects are seen clearly, and hence are possible to annotate, are used. Figure 17 shows an example of when the focus is set wrongly, so that only the thermal infrared worker detects the drone. This issue justifies the multi-sensor approach followed here. Also, cameras not affected by this issue (such as the thermal infrared or the fish-eye) could be used to aid the focus of the video camera.

Comparing the results to other papers, our results are ahead to what is presented in [11], where a mAP of 0.66 achieved, albeit using a detector with drones as the only output class and giving no information about the sensor-to-target distances. Also, we see that the YOLOv2 detector in [19] achieves an F1-score of 0.728 with exactly the same detection threshold and IoU-requirement. This F1-score is just below the results of the thermal infrared and video camera workers. However, one notable difference lies in that the detector in [19] has only one output class. This fact could confirm the doctrine of this work, i.e. that the detectors should also be trained in recognizing object easily confused for being drones. Unfortunately, there is no notation of the sensor-to-target distance other than that “75% of the drones have widths smaller than 100 pixels”. Since the authors implement an original YOLOv2 model from darknet, it is assumed that the input size of the detector is 416×416 pixels. A YOLOv2-architecture with an

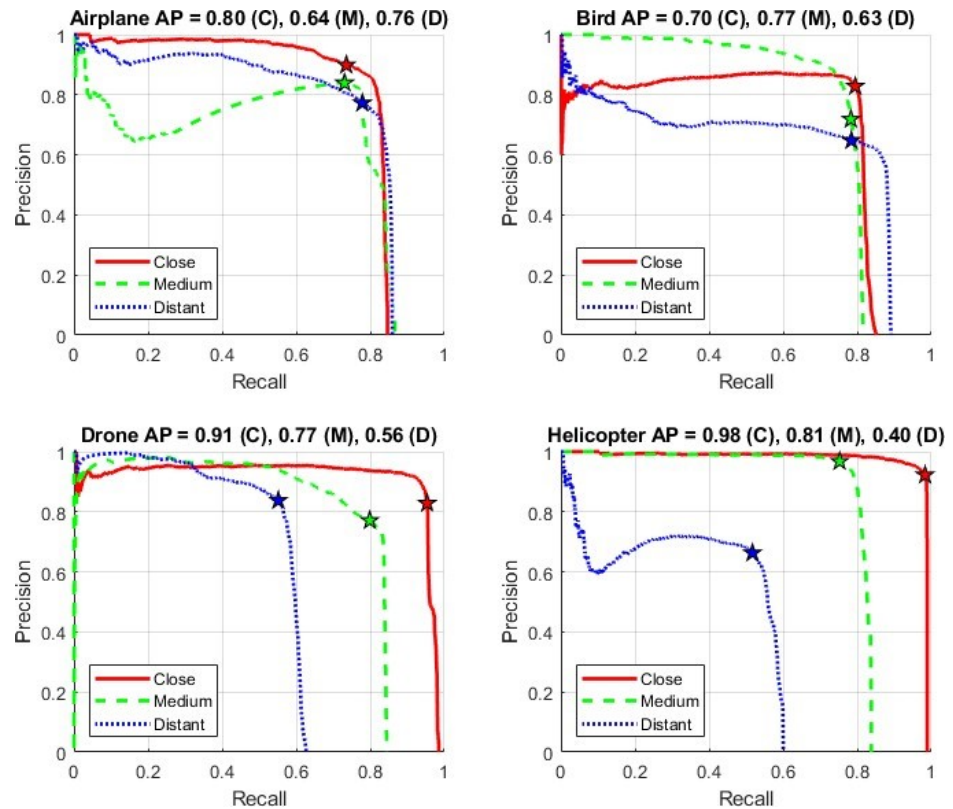


Figure 16. Precision and recall curves with the visible camera. The achieved values with a detection threshold of 0.5 are marked by stars.

input size of 480×480 pixels is implemented in [12]. The detector has two output classes, birds and drones. Based on the presented precision-recall curve, a precision and recall of 0.9 can be achieved at the same time. To summarize this comparison, we provide the performance of the thermal infrared and video camera detectors together with the reported comparable results in Table 8. The table also shows the output classes used.

Table 8. Results from the related works and the thermal infrared and video camera detectors. A = Airplane, B = Bird, D = Drone and H = Helicopter.

Work	Sensor	Results				Classes
		Precision	Recall	F1-score	mAP	
Park et al. [19]	Visible			0.73		D
Liu et al. [21]	Visible	0.99	0.80			A, D, H
Saqib et al. [11]	Visible				0.66	D
Aker and Kalkan. [12]	Visible	~0.9	~0.9			B, D
thermal infrared	Thermal	0.82	0.72	0.76	0.71	A, B, D, H
video camera	Visible	0.81	0.76	0.78	0.73	A, B, D, H

4.3. Fish-Eye Camera Motion Detector (Fcam)

The fish-eye lens camera is included to be able to cover a larger airspace volume than covered by just the field of view of the thermal infrared and video camera. However, the drone detection system is not totally reliant on the fish-eye worker to detect objects of interest,

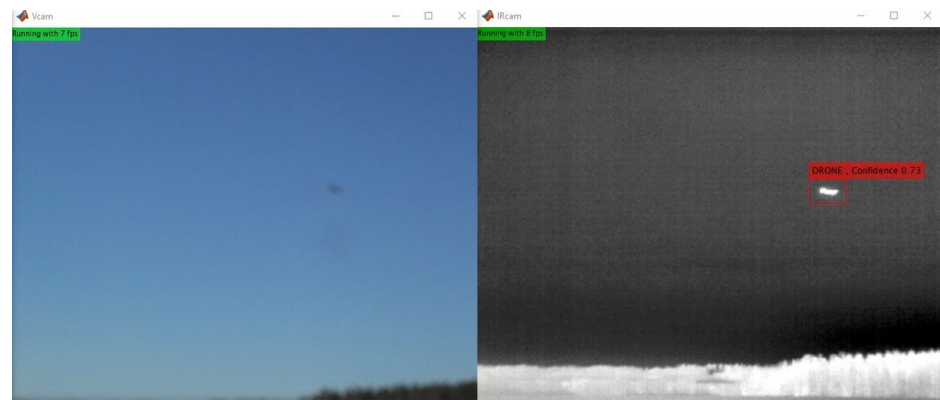


Figure 17. A drone detected only by the thermal infrared sensor since the auto-focus of the video camera is wrongly set.

since the system also include the search programs moving the pan/tilt platform when no other targets are detected. The search programs can easily be turned on or off using the control panel of the GUI.

It was initially observed that the foreground/background-based motion detector of the fish-eye worker was sensitive to objects moving with the wind as shown in Figure 18. The number of false targets has been mitigated by extensive tuning of the image processing operations, the foreground detector, the blob analysis settings and the parameters of the multi-object Kalman filter tracker from [51]. Some of the most critical points in this was first to remove the `imclose` and `imfill` functions that were initially implemented after the `imopen` function in the image processing operations. Furthermore, the minimum background ratio setting of the foreground detector was increased together with the learning rate, so that the GMM more quickly adapts to changing conditions. In the blob analysis settings, the minimum blob area was reduced, so that smaller objects are detectable and a maximum blob area was also implemented. Tuning the parameters of the Kalman filter multi-object tracker was also important. These were altered to make the tracker slower to start new tracks and quicker to terminate them if no moving objects were present at the predicted positions.

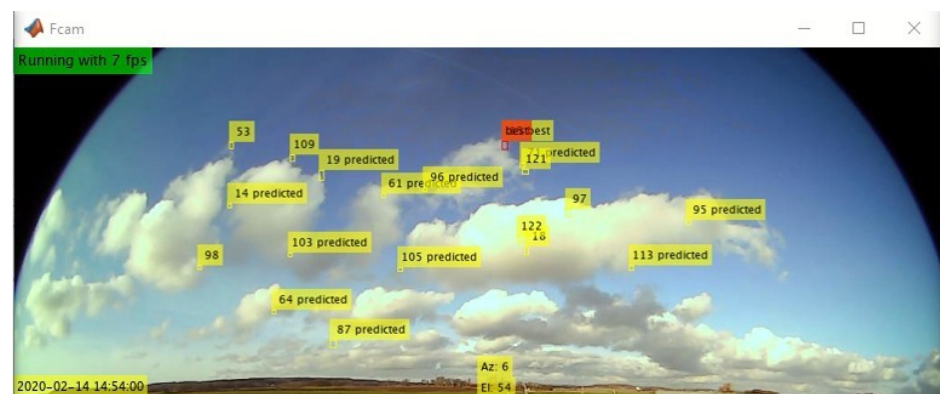


Figure 18. False targets in a fish-eye camera image.

With an image size of 1024×384 , the fish-eye worker moving object detector and tracker has been found, during the evaluation sessions, to be an effective way to assign objects to the pan/tilt platform up to a distance of 50 m against drones. Beyond this distance, the drone appears so small (in pixels) that it is deleted by the `imopen` function. The maximum resolution of the fish-eye camera employed is 3264×2448 , so a greater detection range should theoretically

be achievable. However, using a higher resolution is also more demanding in computational resources, leading to a reduction in the FPS-performance, not only for the fish-eye worker, but also for the other workers. Since the fish-eye lens camera is also complemented by the search program, where the pan/tilt platform can be controlled by the output of the other workers, the choice has been made to settle with this resolution and the limited detection range that follows from this. Figure 19 (left) shows a drone tracked by the fish-eye worker. At this moment the pan/tilt platform is controlled by the output of the fish-eye worker. Just a moment later, as seen at the right of the figure, the drone is detected by the thermal infrared and video camera workers, and the pan/tilt platform is therefore controlled by the thermal infrared worker output.

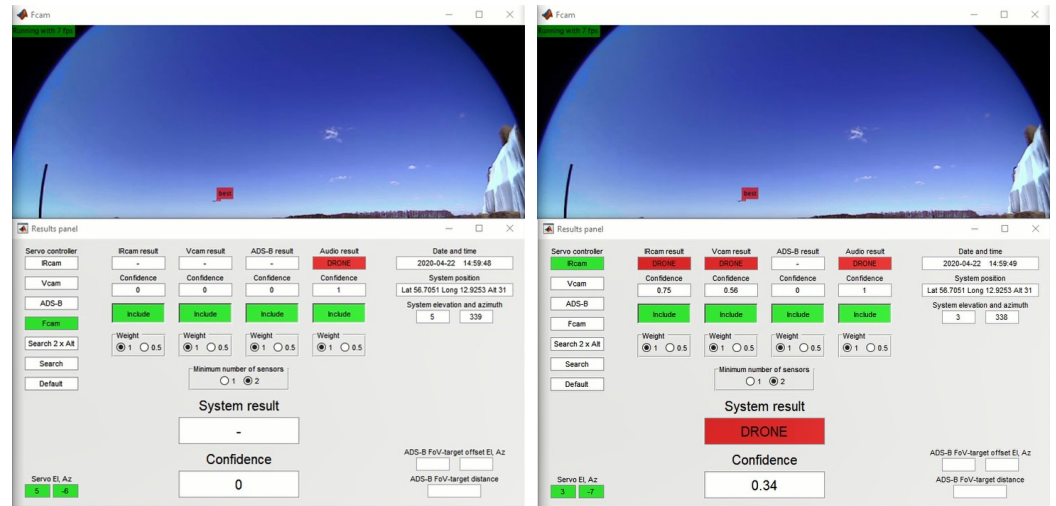


Figure 19. Left: a drone tracked by the fish-eye worker. Right: the drone tracked by the thermal infrared worker just a second later (note the timestamp).

4.4. Microphone

The precision and recall results of the different classes with this detector are shown in Table 9. Against a drone, the practical range of the acoustic sensor is 35–45 m, depending on how the drone is flying. This is in parity with the 50 m of [26], but far from the 160 m against a F450 drone reported in [32] with its much more complex microphone configuration (a 120 elements microphone array).

Table 9. Results with the audio detector. Reprinted with permission from [13].

	drone	helicopter	background	average
Precision	0.9694	0.8482	0.9885	0.9354
Recall	0.9596	0.9596	0.8687	0.9293
F1-score				0.9323

Our average F1-score is 0.9323, which is higher compared to [29], which also uses MFCC features. Out of the three classifier types tested in [29], the one comprising a LSTM-RNN performs the best, with a F1-score of 0.6984. The classification problem in that paper is binary (drone or background). Another paper applying MFCC-features is [30] and Support Vector Machines (SVM) as classifier, with a precision of 0.983. Five output classes are used (drone,

nature daytime, crowd, train passing and street with traffic), and the classification is based on a one-against-one strategy, hence ten binary SVM classifiers are implemented. The final output label is then computed using the max-wins voting principle. The paper [24], on the other hand, applies the Fast Fourier Transform (FFT) to extract features from the audio signals. The results of the audio detector together with results reported in other studies are summarized in Table 10.

Table 10. Results from the related works and the audio detector. D = Drone, H = Helicopter, BG = Background. The work [30] defines four background classes: nature daytime, crowd, train passing and street with traffic.

Work	Results			Classes
	Precision	Recall	F1-score	
Kim et al. [24]	0.88	0.83	0.85	D, BG
Jeon et al. [29]	0.55	0.96	0.70	D, BG
Bernardi et al. [30]	0.98			D, BG
audio worker	0.94	0.93	0.93	D, H, BG

4.5. Radar Module

From the datasheet of the K-MD2 [48], we have that it can detect a person with a Radar Cross Section (RCS) of 1 m^2 up to a distance of 100 m. Since we have from [33] that the RCS of the F450 drone is 0.02 m^2 , it is straight forward to calculate that, theoretically, the F450 should be possible to detect up to a distance of $100 \times \sqrt[4]{0.02/1} = 37.6 \text{ m}$. Furthermore, given that the micro-doppler echoes from the rotors are 20 dB below that of the drone body, these should be detectable up to a distance of $100 \times \sqrt[4]{0.02/1 \times 100} = 11.9 \text{ m}$.

Practically, we have observed that the F450 drone is detected and tracked by the K-MD2 up to a maximum distance of 24 m. This is however the maximum recorded distance, and it is observed that the drone is generally detected up to a distance of 18 m. Due to the short practical detection range of the radar module, it is not included in the drone detection system of this work. The micro-doppler signature can also be detected at short distances, as shown in Figure 20. Corresponding range-doppler plots showing the micro-doppler of flying drones can be found in [38] and [39] as well. Compared to the echo of a person walking in front of the radar, as we can see at the bottom of the figure, no such micro-doppler signature is present in that case.

4.6. Sensor Fusion

We investigated the choice of early or late sensor fusion. By early sensor fusion, we mean to fuse the images from the thermal infrared and video cameras before processing them in a detector and classifier. Late sensor fusion will, in this case, be to combine the output results from the separate detectors running on each camera stream. When implementing early sensor fusion, the pixel-to-pixel matching of the images turned out to be the biggest issue. Even if this is possible to do in a static scenario, it turned out not to be a feasible solution against moving objects, such as drones, with the available equipment. This stems from the small but still noticeable difference in latency between the two cameras. This is the motive for the implementation of late sensor fusion in the drone detection system of this work. An interesting early sensor fusion method is also found in [22] where the image from the narrow-angle camera is inserted in the image from the wide-angle camera and then processed by a single YOLO detector. It is a bit unclear how they avoid situations when the inserted image obscure the object found in the wide-angle image. In [9], they implement sensor fusion using a trained

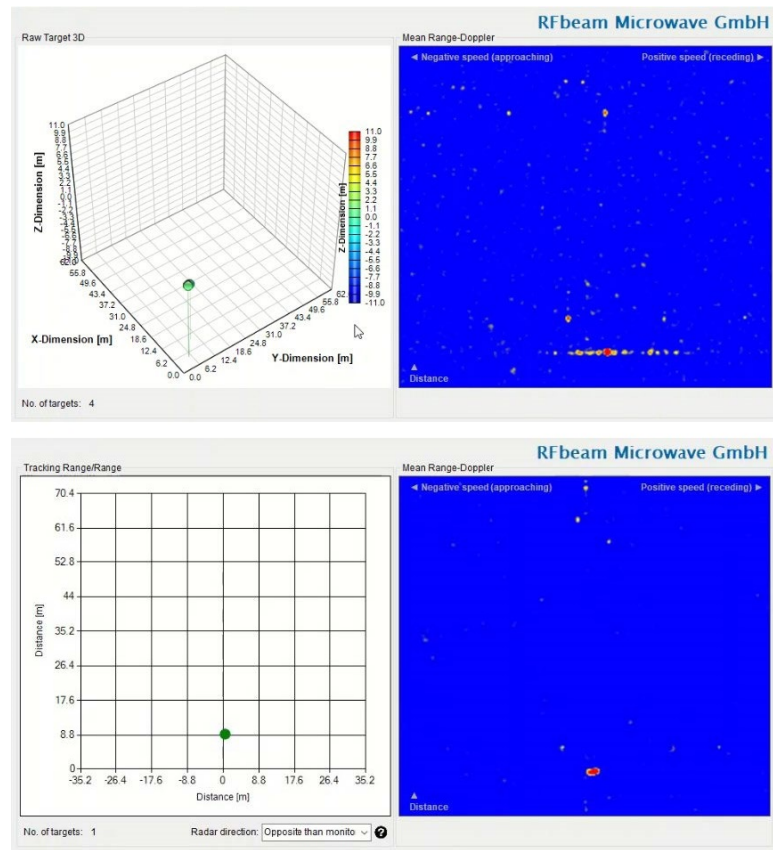


Figure 20. Top: micro-doppler signature of the F450 drone. Bottom: echo of a person walking in front of the radar module.

network. To do so here would likely require much more training data, not only on individual sensor level, but especially on a system level. Such amounts of data have not been possible to achieve within the scope of this work.

The sensor fusion implemented consists of utilizing the class outputs and the confidence scores of the available sensors, smoothing their result over time. To do so, every time the main script polls the worker's queues, it puts the results in a 4×4 matrix, organized so that each class is a column and each sensor is a row. The values of the matrix depend not only on the class label and the confidence, but also on the setting of which sensors to include and the weight of the specific sensor, i.e. how much we trust it at the moment. A new 1×4 matrix is then formed by column-wise sum. This array is in turn placed as a new row in a 10×4 first-in-first-out time-smoothing matrix. Since we have close to ten FPS from the workers, this will be the results of approximately the last second. Once again the 10 columns are summarized into a 1×4 matrix, and the column with the highest value will be the output system class. The system output confidence is calculated by normalizing the value found to be highest over the number of sensors included at the moment. An additional condition before presenting the system result is also that the minimum number of sensors that detects any object has to fulfil the GUI-setting, as shown in Figure 21. The figure also shows an example of how sensor fusion is enabled in the GUI, which includes choice of the weight for each sensor and the minimum number required. With such dynamical setting, it is possible to use not only the OR-function, as in [10], but more sophisticated variants by varying the number of sensors included and required for detection, including their weights.

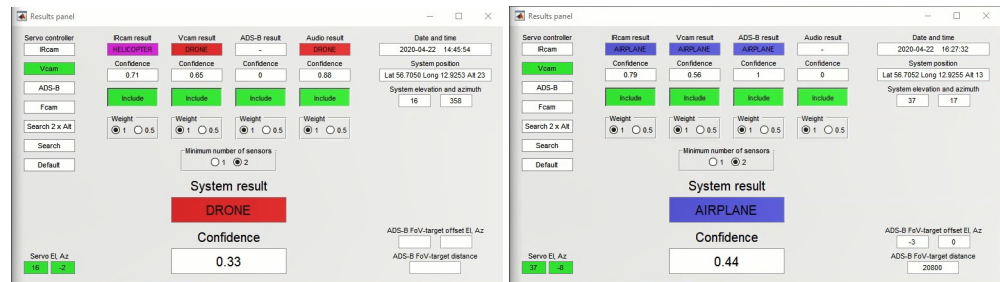


Figure 21. Two examples of sensor fusion results. Pictures originally appearing in [47] and published in [13]. Reprinted with permission.

Evaluating the fusion turned out to be harder than expected, since this research was mostly done during the COVID19 pandemic. For example, regular flights at the airports considered in this work were cancelled, hence the possibility for a thorough system evaluation against airplanes. Using the screen recorder, it is possible to do a frame-by-frame analysis of a typical drone detection, as shown in Figure 22 (left). The “servo” column indicates the current servo controlling sensor and the “Fcam” column specifies if the fish-eye camera motion detector is tracking the drone. The respective class output labels of each worker are shown in the rest of the columns. Note that the system output is more stable and lasts for more frames than the thermal infrared and video camera individually, indicating the benefit of the sensor fusion. Since there is no information from the ADS-B receiver in this case, that column has been omitted from the table. Figure 8 above is the third frame from 14:46:18. As it can be seen, the thermal infrared, video camera and audio workers detect and classify the drone correctly. The fish-eye camera worker is also tracking the drone, and the pan/tilt platform at this moment is being controlled by the thermal infrared worker.

Time	Servo	Fcam	IRcam	Vcam	Audio	System
14:46:17	Fcam	✓			DRONE	
14:46:17	Fcam	✓			DRONE	
14:46:17	IRcam	✓	AIRPLANE		DRONE	DRONE
14:46:17	IRcam	✓	AIRPLANE		DRONE	DRONE
14:46:17	IRcam	✓	AIRPLANE		DRONE	DRONE
14:46:17	IRcam	✓	AIRPLANE		DRONE	DRONE
14:46:17	IRcam	✓		DRONE	DRONE	DRONE
14:46:17	Vcam	✓		DRONE	DRONE	DRONE
14:46:18	Vcam	✓		DRONE	DRONE	DRONE
14:46:18	IRcam	✓	DRONE	DRONE	DRONE	DRONE
14:46:18	IRcam	✓	DRONE	DRONE	DRONE	DRONE
14:46:18	IRcam	✓	DRONE	DRONE	DRONE	DRONE
14:46:18	IRcam	✓	DRONE	DRONE	DRONE	DRONE
14:46:18	IRcam	✓	DRONE	DRONE	DRONE	DRONE
14:46:18	IRcam	✓	DRONE	DRONE	DRONE	DRONE
14:46:18	IRcam	✓	DRONE	DRONE	DRONE	DRONE
14:46:18	IRcam	✓	DRONE	DRONE	DRONE	DRONE
14:46:18	Vcam	✓		DRONE	DRONE	DRONE
14:46:19	Vcam	✓		DRONE	DRONE	DRONE
14:46:19	IRcam	✓	HELICOPTER	DRONE	DRONE	DRONE
14:46:19	IRcam	✓		DRONE	DRONE	DRONE
14:46:19	IRcam	✓	BIRD	DRONE	DRONE	DRONE
14:46:19	IRcam	✓	BIRD	HELICOPTER	DRONE	DRONE
14:46:19	IRcam	✓			HELICOPTER	
14:46:19	Fcam	✓			HELICOPTER	

Time	IRcam	Vcam	Object	Output label
00:31	✓		Cloud	BIRD
01:10	✓		Insect	AIRPLANE
01:46	✓		Cloud	HELICOPTER
02:05	✓		Insect	BIRD
02:25	✓		Cloud	AIRPLANE
02:34	✓		Insect	BIRD
02:58		✓	Cloud	AIRPLANE
03:00	✓		Cloud	BIRD
03:12	✓		Insect	AIRPLANE
03:13	✓		Insect	AIRPLANE
03:38	✓		Cloud	AIRPLANE
04:26		✓	Insect	BIRD
05:11	✓		Cloud	BIRD
05:12	✓		Cloud	AIRPLANE
05:15	✓		Cloud	BIRD
05:48	✓		Cloud	BIRD
06:11	✓		Cloud	BIRD
07:04	✓		Cloud	AIRPLANE
07:34	✓		Cloud	BIRD
07:38	✓		Cloud	BIRD
07:39	✓		Cloud	BIRD
08:11	✓		Cloud	DRONE
08:30	✓		Insect	BIRD
08:47	✓		Cloud	DRONE
08:49	✓		Cloud	DRONE
08:51	✓		Insect	BIRD
09:29		✓	Insect	BIRD
09:30	✓		Cloud	BIRD
09:31	✓		Insect	BIRD
09:33	✓		Cloud	BIRD
09:37	✓		Cloud	AIRPLANE

Figure 22. Left: frame-by-frame analysis of drone detection during one evaluation session. Right: false detections appearing in a ten minutes long section of screen recording from an evaluation session, including the type of object causing the false detection. Pictures originally appearing in [47] and published in [13]. Reprinted with permission.

As an attempt to measure the efficiency of the sensor fusion, we can consider occasions such as the one described in Figure 22 (left) as being a *detection opportunity*. If we define this to be when the drone is continuously observable in the field of view of the thermal infrared and video cameras, and hence possible for the system (including the audio classifier) to analyse and track, we have carried out 73 such opportunities in the screen recordings from the evaluation sessions. The duration of the individual detection opportunities is from just fractions of a second up to 28 seconds. This is highly dependent on how the drone is flying and if the system is able to track the drone or not. We can see that Figure 22 (left) describes the frame-by-frame analysis of a detection opportunity lasting for three seconds. Comparing the system results after the sensor fusion with the output from the respective sensors, we can observe that the system outputs a drone classification at some time in 78% of the detection opportunities. Closest to this is the performance of the video camera detector that outputs a drone classification in 67% of the opportunities.

We have also looked at the system behaviour without a drone flying in front of it in order to analyse false detections. To do this, a ten minutes long section of videos from the evaluation sessions was reviewed frame-by-frame. Figure 22 (right) shows the timestamps, sensor types, causes of false detection, and resulting output labels. Setting the minimum number of sensors option to two prevents all the false detections in the figure from becoming false detections on a system level. The false detections caused by insects flying just in front of the sensors are very short-lived, while the ones caused by clouds can last longer, up to several seconds. Figure 23 shows the false detections of the thermal infrared at 02:34 and the video camera at 02:58. As described earlier, the individual weaknesses observed for the primary sensors are sensitivity to clouds (thermal infrared) and autofocus problem (video camera). However, the fusion detection pipeline shows that such individual shortcomings can be overcome with a multi-sensor solution.

Some other screenshots from the system evaluation sessions and some complementary interesting observations are also pointed out in Appendix A.



Figure 23. False detections of the thermal infrared at 02:34 and the video camera at 02:58 indicated in Figure 22 (right).

5. Conclusions

The increased use of drones for many types of recreational and professional purposes is creating concerns about safety and security of premises where such vehicles may create risk situations or compromise security. Here, we explore the design of a multi-sensor drone detection system that employs state-of-the-art feature extraction and machine learning techniques, e.g. YOLOv2 detector [20], GMM background subtraction [23], Kalman filters [51], MFCC audio features or LSTM classifiers [31]. We employ a common video camera and audio microphone, complemented with a thermal infrared camera. These two cameras are steered towards potential objects of interest with a fish-eye lens camera which has a wider field of view and is used to detect moving objects at once over a bigger portion of the sky. We also include

an ADS-B receiver, which allows to track cooperative aircrafts that broadcast its vehicle type, and a GPS receiver. We have also evaluated a radar module, which has been finally discarded due to its very short practical range. The sensors are all placed on a pan/tilt platform that is mounted on a standard surveyors tripod. This allows easy deployment of the solution outdoors and portability, since the system can be disassembled into a few large parts and placed in a transport box.

The performance of the individual sensors are evaluated in terms of precision, recall, F1-score and mean average precision (mAP). With machine learning techniques, we observe that thermal infrared sensors are suitable for the drone detection task. The infrared detector achieves an F1-score of 0.7601, showing similar performance as the visible video detector with an F1-score of 0.7849. The audio classifier achieves an F1-score of 0.9323. By sensor fusion, we also make the detection and classification more robust than any of the sensors individually, showing as well the efficiency of sensor fusion as a mean to mitigate false detections. Another novelty is the investigation of detection performance as a function of the sensor-to-target distance. We also contribute with a multi-sensor dataset, which overcome the lack of publicly available data for this task. Apart from the feasibility of the sensors employed, specially of the thermal infrared one, our dataset also use an expanded number of target classes compared to related papers. Our dataset is also especially suited for the comparison of infrared and visible video detectors due to the similarities in conditions and target types in the set. To the best of our knowledge, we are also the first to explore the benefits of including ADS-B data to better separate targets prone to be mistaken for drones.

A future research could be to implement a distance estimation function based on the output from the detectors. Such research could also include the investigation of distributed sensors, and to further make use of the temporal dimension to separate drones from other targets based on the behaviour over time as they are tracked by the system. Another direction is to implement the YOLO detector in the fish-eye camera, although this would demand a training dataset, or skewing images of the video camera to match the fish-eye lens distortion. It would also be of interest to use YOLO v3 instead, since it is more efficient in detecting small objects according to [22]. The performance of the audio classifier with respect to the sensor-to-target distance could also be explored in the same way than the video sensors.

Having a radar with a useful range would have contributed significantly to the system results, since it is the only one of the available sensors being able to measure the distance to the target efficiently. Likewise, it would be interesting to test the system against a drone equipped with a transponder to see the performance of the ADS-B worker at a short distance. Such transponders weigh as little as 20 grams [60]. However, the price of such equipment (~3k€) is still an issue for the non-professional drone user. Since ADS-B information is included in the system, this could also be implemented in the form of ground truth for an online learning feature. Images of ADS-B targets could be saved, and on regular intervals, the detectors would be retrained using these additional images. To further enlarge the training data set all images of detected objects could be saved and annotated manually at a later stage.

This work can also be useful in other areas. One example is road traffic surveillance, since most parts and scripts (except the ADS-B receiver) are applicable after appropriate retraining to detect and track road vulnerable users (pedestrians), vehicles, etc. and even specific vehicle types such as light ones (bikes, motorcycles) or heavy ones (trucks). Another application involving detection of people is surveillance of large areas where access is restricted and operator monitoring can be very resource-consuming if not automated, such as outdoors.

Author Contributions: This work has been carried out by Fredrik Svanström under the supervision of Fernando Alonso-Fernandez and Cristofer Englund in the context of his Master Thesis at Halmstad University (Master's Programme in Embedded and Intelligent Systems). The thesis is available at [47]. Fredrik Svanström: Conceptualization, Methodology, Investigation, Data curation, Writing –review &

editing; Fernando Alonso-Fernandez: Conceptualization, Supervision, Funding acquisition, Writing – original draft; Cristofer Englund: Conceptualization, Supervision, Writing – review & editing.

Funding: Author F. A.-F. thanks the Swedish Research Council (VR) for funding his research. Authors F. A.-F. and C. E. thank the Swedish Innovation Agency (VINNOVA) for funding their research.

Data Availability Statement: The data used in this paper is fully described in [55] and publicly available at [56].

Conflicts of Interest: The authors declare no conflict of interest.

Abbreviations

The following abbreviations are used in this manuscript:

MDPI	Multidisciplinary Digital Publishing Institute
DOAJ	Directory of open access journals
TLA	Three letter acronym
LD	Linear dichroism

Appendix A. Complementary screenshots and observations to the sensor fusion evaluation sessions

In this section, some screenshots from the system evaluation sessions and some interesting observations are pointed out. The images also indicate the FPS performance. The system is able to process 6 FPS or more from all cameras and over 10 processing cycles for the input audio stream per second. To be able to evaluate the system performance, a screen recording software has also been running on the computer at the same time as the system software.

The ideal situation is of course that all the sensors output the correct classification of the detected target and that the object is tracked by the fish-eye camera. This is, however, far from the case at all times. Nevertheless, after the sensor fusion, the system output class is observed to be robust, as shown in Figure A1 and A2, where the video and thermal infrared cameras classifies the drone incorrectly, but still with a correct system output.

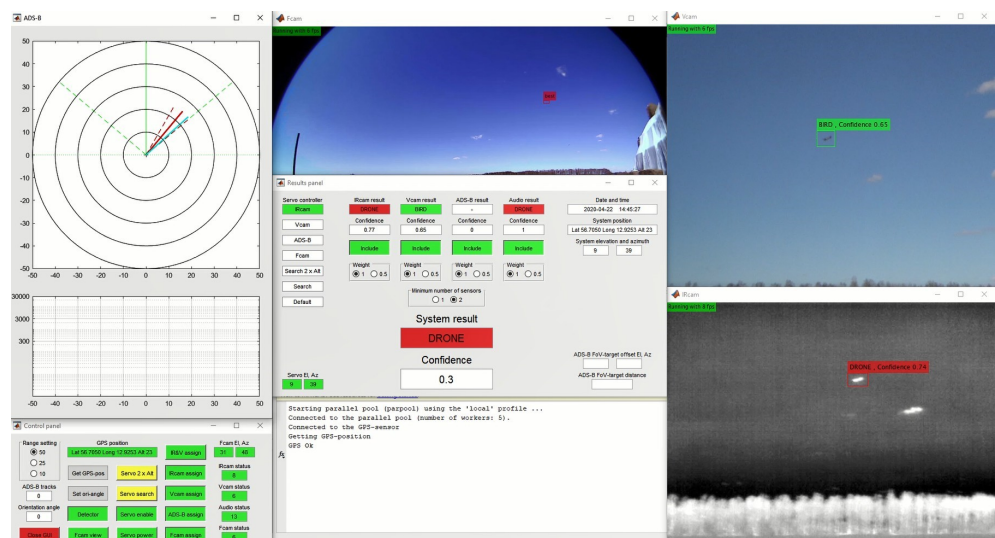


Figure A1. A correct system output even if the video camera classifies the drone as being a bird.

Since the output class depends on the confidence score, the result is sometimes also the opposite, as shown in Figure A3, so that a very confident sensor (audio) causes the system output to be wrong. If this turns out to be frequent, the weight of the sensor can easily be

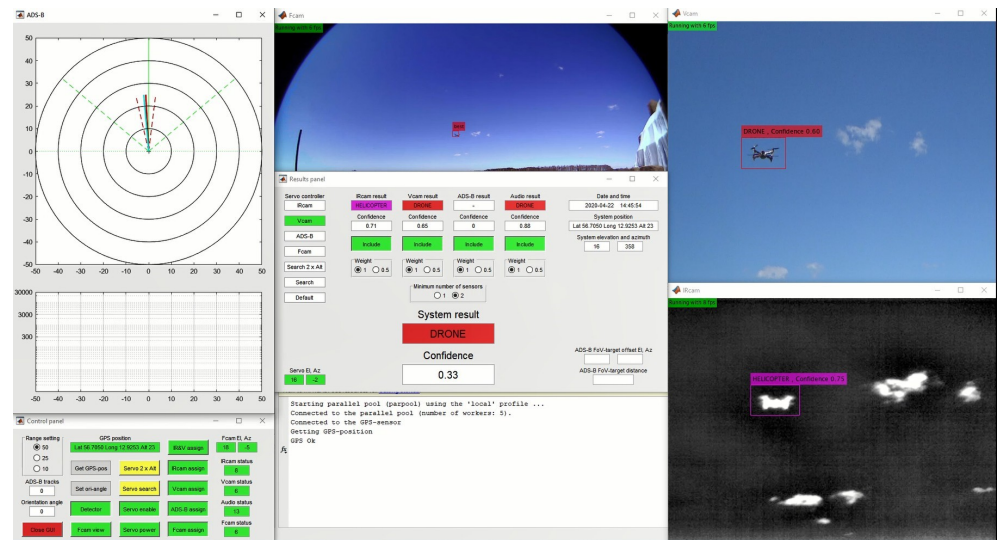


Figure A2. A correct system output even if the thermal infrared camera classifies the drone as being a helicopter.

adjusted, or the sensor can be excluded completely from the system result. The time smoothing procedure of the sensor fusion will also reduce the effect of an occasional misclassification, so that the system output stays correct, as can be seen in Figure A4. Naturally, there are also times when all sensors are wrong, as evident in Figure A5.

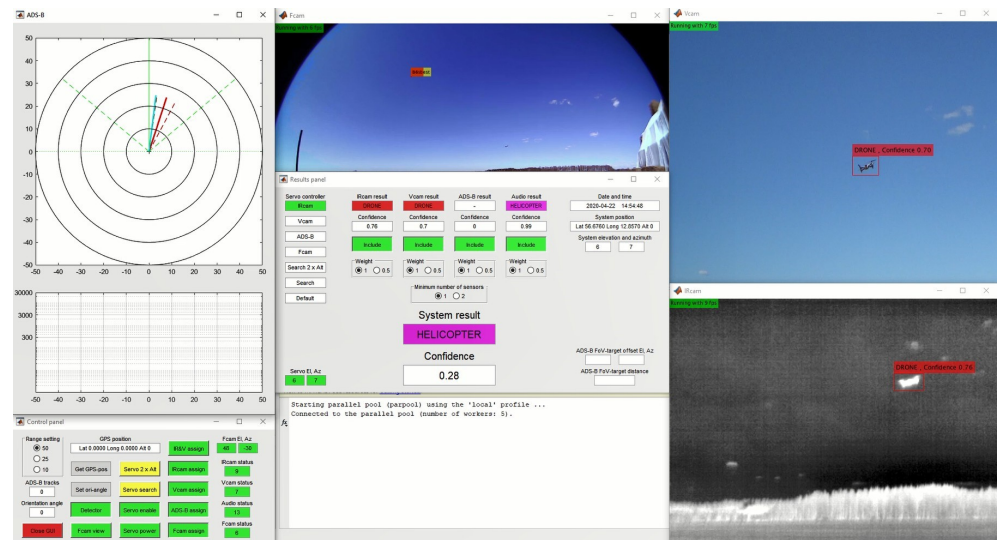


Figure A3. The high confidence score of the audio classifier cases the system output to be incorrect just as the audio output.

To the best of our knowledge, the inclusion of an ADS-B receiver in a drone detection system has not yet been described in the scientific literature, so it is also of interest to see how this information is utilized. In Figure A6, an airplane is detected and classified at a sloping distance of more than 35000 m. The ADS-B information is guiding the pan/tilt platform in the direction of the airplane, so that it can be detected by the video camera. At this distance even a large commercial airplane is only about 1.4 pixels, and hence well below the detection limit of the DRI-criteria. The reason behind the fact that the ADS-B FoV-target distance display is

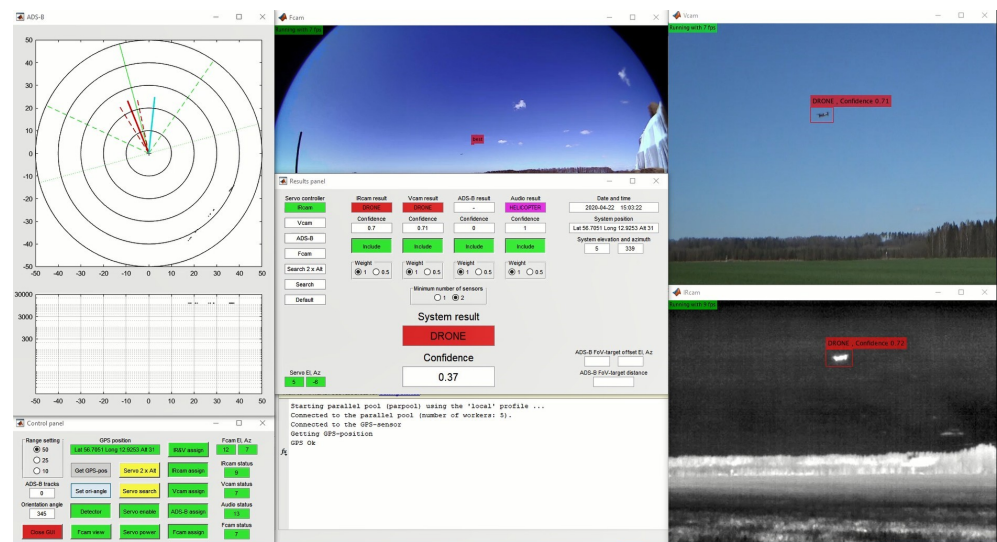


Figure A4. The time smoothing part of the sensor fusion reduces the effect of an occasional misclassification, even if that has a high confidence scores.

empty is that the main script will not present that information until the target is within 30000 m horizontal distance. This limit is set based on the assumption that no target beyond 30000 m should be detectable, an assumption that clearly turned out to be wrong.

Looking at Figure A7, we can see that when the airplane comes within 30000 m horizontal distance from the system the ADS-B information will appear in the results panel. At this moment, the sloping distance is 32000 m and the offset between the camera direction and the calculated one is zero. Moreover, since the system has not yet received the vehicle category information at this moment the target is marked with a square in the ADS-B presentation area, and the confidence score of the ADS-B result is 0.75. The next interesting event, shown in Figure A8, is when the system receives the vehicle category message. To indicate this, the symbol in the ADS-B presentation is changed to a circle, and the confidence is set to one, since we are now sure that it is an airplane. At a distance of 20800 m, it is also detected and classified correctly by the thermal infrared worker, as shown in Figure A9.

References

1. Mohsan, S.A.H.; Khan, M.A.; Noor, F.; Ullah, I.; Alsharif, M.H. Towards the Unmanned Aerial Vehicles (UAVs): A Comprehensive Review. *Drones* **2022**, *6*. <https://doi.org/10.3390/drones6060147>.
2. The World Air Sports Federation FAI. World Drone Racing Championship. <https://www.fai.org/world-cups/drone-racing-2020> **2020**.
3. Aviation International News. What happens when a drone hits an airplane wing? About the University of Dayton research institute. <https://www.youtube.com/watch?v=QH0V7kp-xg0> **2020**.
4. List of UAV-related incidents. https://en.wikipedia.org/wiki/List_of_UAV-related_incidents **2022**.
5. Taha, B.; Shoufan, A. Machine Learning-Based Drone Detection and Classification: State-of-the-Art in Research. *IEEE Access* **2019**, *7*, 138669–138682.
6. Google Trends. <https://trends.google.com/trends/explore?date=all&q=dronedetection> **2020**.
7. Guvenc, I.; Koohifar, F.; Singh, S.; Sichitiu, M.L.; Matolak, D. Detection, Tracking, and Interdiction for Amateur Drones. *IEEE Communications Magazine* **2018**, *56*, 75–81.
8. Samaras, S.; Diamantidou, E.; Ataloglou, D.; Sakellariou, N.; Vafeiadis, A.; Magoulaitis, V.; Lalas, A.; Dimou, A.; Zarpalas, D.; Votis, K.; et al. Deep Learning on Multi Sensor Data for Counter UAV Applications—A Systematic Review. *Sensors* **2019**, *19*, 4837. <https://doi.org/10.3390/s19224837>.
9. Diamantidou, E.; Lalas, A.; Votis, K.; Tzovaras, D. Multimodal Deep Learning Framework for Enhanced Accuracy of UAV Detection. In Proceedings of the Computer Vision Systems; Tzovaras, D.; Giakoumis, D.; Vincze, M.; Argyros, A., Eds.; Springer International Publishing: Cham, 2019; pp. 768–777.

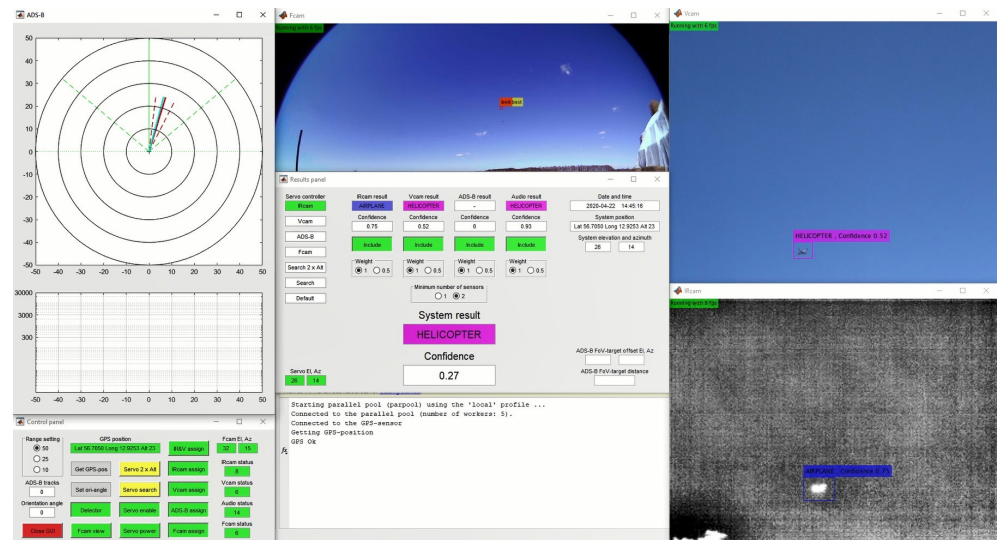


Figure A5. The drone is misclassified by several sensors at the same time.

10. Shi, X.; Yang, C.; Xie, W.; Liang, C.; Shi, Z.; Chen, J. Anti-Drone System with Multiple Surveillance Technologies: Architecture, Implementation, and Challenges. *IEEE Communications Magazine* **2018**, *56*, 68–74.
11. Saqib, M.; Daud Khan, S.; Sharma, N.; Blumenstein, M. A study on detecting drones using deep convolutional neural networks. In Proceedings of the 14th IEEE International Conference on Advanced Video and Signal Based Surveillance (AVSS), 2017, pp. 1–5.
12. Aker, C.; Kalkan, S. Using deep networks for drone detection. In Proceedings of the 14th IEEE International Conference on Advanced Video and Signal Based Surveillance (AVSS), 2017, pp. 1–6.
13. Svanström, F.; Englund, C.; Alonso-Fernandez, F. Real-Time Drone Detection and Tracking With Visible, Thermal and Acoustic Sensors. In Proceedings of the 2020 25th International Conference on Pattern Recognition (ICPR), 2021, pp. 7265–7272. <https://doi.org/10.1109/ICPR48806.2021.9413241>.
14. Boddhu, S.K.; McCartney, M.; Ceccopieri, O.; Williams, R.L. A collaborative smartphone sensing platform for detecting and tracking hostile drones. In Proceedings of the Ground / Air Multisensor Interoperability, Integration, and Networking for Persistent ISR IV; Pham, T.; Kolodny, M.A.; Priddy, K.L., Eds. International Society for Optics and Photonics, SPIE, 2013, Vol. 8742, pp. 293 – 303. <https://doi.org/10.1117/12.2014530>.
15. Guard From Above BV. <https://guardfromabove.com> **2020**.
16. Andrašić, P.; Radišić, T.; Muštra, M.; Ivošević, J. Night-time Detection of UAVs using Thermal Infrared Camera. *Transportation Research Procedia* **2017**, *28*, 183 – 190. INAIR 2017, <https://doi.org/https://doi.org/10.1016/j.trpro.2017.12.184>.
17. Wang, Y.; Chen, Y.; Choi, J.; Kuo, C.C.J. Towards Visible and Thermal Drone Monitoring with Convolutional Neural Networks. *APSIPA Transactions on Signal and Information Processing* **2019**, *8*, e5. <https://doi.org/10.1017/ATSIP.2018.30>.
18. Wu, M.; Xie, W.; Shi, X.; Shao, P.; Shi, Z. Real-Time Drone Detection Using Deep Learning Approach. In Proceedings of the Machine Learning and Intelligent Communications; Meng, L.; Zhang, Y., Eds.; Springer International Publishing: Cham, 2018; pp. 22–32.
19. Park, J.; Kim, D.H.; Shin, Y.S.; Lee, S. A comparison of convolutional object detectors for real-time drone tracking using a PTZ camera. In Proceedings of the 2017 17th International Conference on Control, Automation and Systems (ICCAS), 2017, pp. 696–699.
20. Redmon, J.; Farhadi, A. YOLO9000: Better, Faster, Stronger. In Proceedings of the IEEE Conference on Computer Vision and Pattern Recognition (CVPR), 2017, pp. 6517–6525.
21. Liu, H.; Qu, F.; Liu, Y.; Zhao, W.; Chen, Y. A drone detection with aircraft classification based on a camera array. *IOP Conference Series: Materials Science and Engineering* **2018**, *322*, 052005. <https://doi.org/10.1088/1757-899x/322/5/052005>.
22. Unlu, E.; Zenou, E.; Riviere, N.; Dupouy, P.E. Deep learning-based strategies for the detection and tracking of drones using several cameras. *IPSJ T Comput Vis Appl* **2019**, *11*.
23. Stauffer, C.; Grimson, W. Adaptive background mixture models for real-time tracking. In Proceedings of the Proceedings. 1999 IEEE Computer Society Conference on Computer Vision and Pattern Recognition (Cat. No PR00149), 1999, Vol. 2, pp. 246–252 Vol. 2. <https://doi.org/10.1109/CVPR.1999.784637>.
24. Kim, J.; Park, C.; Ahn, J.; Ko, Y.; Park, J.; Gallagher, J.C. Real-time UAV sound detection and analysis system. In Proceedings of the IEEE Sensors Applications Symposium (SAS), 2017, pp. 1–5.
25. Siriphun, N.; Kashihara, S.; Fall, D.; Khurat, A. Distinguishing Drone Types Based on Acoustic Wave by IoT Device. In Proceedings of the 22nd International Computer Science and Engineering Conference (ICSEC), 2018, pp. 1–4.

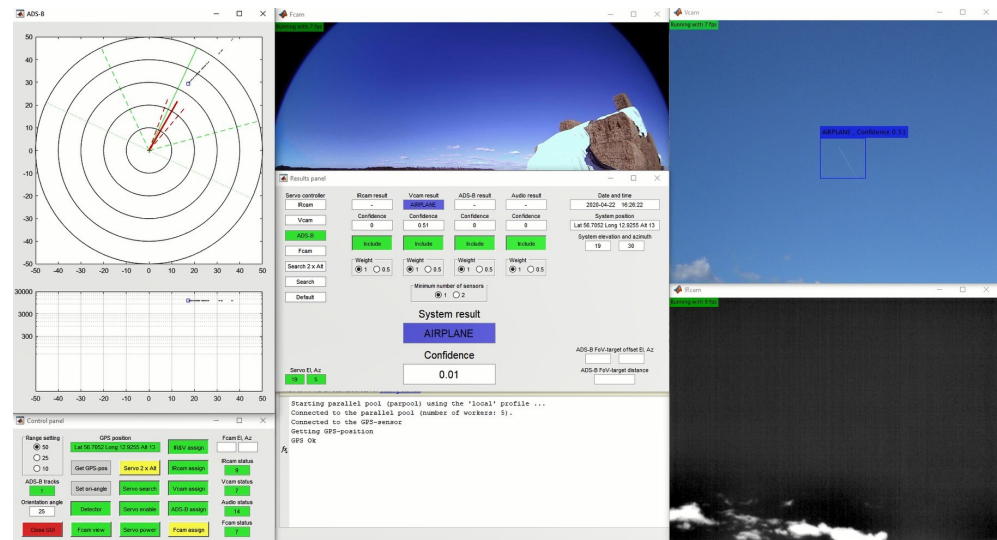


Figure A6. An airplane detected and classified correctly by the video camera worker at a sloping distance of more than 35000 m. See the text for details.

26. Park, S.; Shin, S.; Kim, Y.; Matson, E.T.; Lee, K.; Kolodzy, P.J.; Slater, J.C.; Scherreik, M.; Sam, M.; Gallagher, J.C.; et al. Combination of radar and audio sensors for identification of rotor-type Unmanned Aerial Vehicles (UAVs). In Proceedings of the IEEE SENSORS, 2015, pp. 1–4.
27. Anwar, M.Z.; Kaleem, Z.; Jamalipour, A. Machine Learning Inspired Sound-Based Amateur Drone Detection for Public Safety Applications. *IEEE Transactions on Vehicular Technology* **2019**, *68*, 2526–2534.
28. Liu, H.; Wei, Z.; Chen, Y.; Pan, J.; Lin, L.; Ren, Y. Drone Detection Based on an Audio-Assisted Camera Array. In Proceedings of the IEEE Third International Conference on Multimedia Big Data (BigMM), 2017, pp. 402–406.
29. Jeon, S.; Shin, J.; Lee, Y.; Kim, W.; Kwon, Y.; Yang, H. Empirical study of drone sound detection in real-life environment with deep neural networks. In Proceedings of the 25th European Signal Processing Conference (EUSIPCO), 2017, pp. 1858–1862.
30. Bernardini, A.; Mangiatordi, F.; Pallotti, E.; Capodiferro, L. Drone detection by acoustic signature identification. *Electronic Imaging* **2017**, *2017*, 60–64.
31. Hochreiter, S.; Schmidhuber, J. Long Short-Term Memory. *Neural Computation* **1997**, *9*, 1735–1780, [<https://direct.mit.edu/neco/article-pdf/9/8/1735/813796/neco.1997.9.8.1735.pdf>]. <https://doi.org/10.1162/neco.1997.9.8.1735>.
32. Busset, J.; Perrodin, F.; Wellig, P.; Ott, B.; Heutschi, K.; Rühl, T.; Nussbaumer, T. Detection and tracking of drones using advanced acoustic cameras. In Proceedings of the Unmanned/Unattended Sensors and Sensor Networks XI; and Advanced Free-Space Optical Communication Techniques and Applications; Carapezza, E.M.; Datskos, P.G.; Tsamis, C.; Laycock, L.; White, H.J., Eds. International Society for Optics and Photonics, SPIE, 2015, Vol. 9647, pp. 53 – 60. <https://doi.org/10.1117/12.2194309>.
33. Patel, J.S.; Fioranelli, F.; Anderson, D. Review of radar classification and RCS characterisation techniques for small UAVs or drones. *IET Radar, Sonar Navigation* **2018**, *12*, 911–919.
34. Herschfelt, A.; Birtcher, C.R.; Gutierrez, R.M.; Rong, Y.; Yu, H.; Balanis, C.A.; Bliss, D.W. Consumer-grade drone radar cross-section and micro-Doppler phenomenology. In Proceedings of the IEEE Radar Conference (RadarConf), 2017, pp. 0981–0985.
35. Gong, J.; Yan, J.; Li, D.; Kong, D.; Hu, H. Interference of Radar Detection of Drones by Birds. *Progress In Electromagnetics Research M* **2019**, *81*, 1–11.
36. Fuhrmann, L.; Biallawons, O.; Klare, J.; Panhuber, R.; Klenke, R.; Ender, J. Micro-Doppler analysis and classification of UAVs at Ka band. In Proceedings of the 18th International Radar Symposium (IRS), 2017, pp. 1–9.
37. Björklund, S. Target Detection and Classification of Small Drones by Boosting on Radar Micro-Doppler. In Proceedings of the 15th European Radar Conference (EuRAD), 2018, pp. 182–185.
38. Drozdowicz, J.; Wielgo, M.; Samczynski, P.; Kulpa, K.; Krzonkalla, J.; Mordzonek, M.; Bryl, M.; Jakielaszek, Z. 35 GHz FMCW drone detection system. In Proceedings of the 2016 17th International Radar Symposium (IRS), 2016, pp. 1–4.
39. Rahman, S.; Robertson, D. Radar micro-Doppler signatures of drones and birds at K-band and W-band. *Scientific Reports* **2018**, *8*. The authors acknowledge the funding received from the Science and Technology Facilities Council which has supported this work under grant ST/N006569/1, <https://doi.org/10.1038/s41598-018-35880-9>.
40. Birnbach, S.; Baker, R.; Martinovic, I. Wi-fly?: Detecting privacy invasion attacks by consumer drones. In Proceedings of the NDSS Symposium, 2017, pp. 1–4.

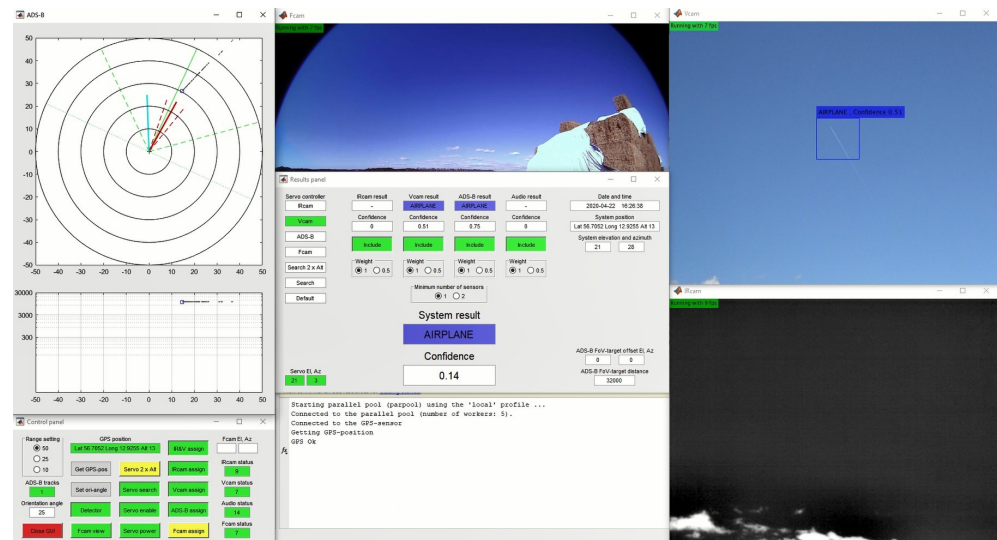


Figure A7. When the airplane is within 30000 m horizontal distance the ADS-B information is presented in the results panel.

41. Shorten, D.; Williams, A.; Srivastava, S.; Murray, J.C. Localisation of Drone Signals from RF Signals Using a Deep Learning Approach. In Proceedings of the Proceedings of the International Conference on Pattern Recognition and Artificial Intelligence; Association for Computing Machinery: New York, NY, USA, 2018; PRAI 2018, p. 89–97. <https://doi.org/10.1145/3243250.3243272>.
42. Ezuma, M.; Erden, F.; Kumar Anjinappa, C.; Ozdemir, O.; Guvenc, I. Detection and Classification of UAVs Using RF Fingerprints in the Presence of Wi-Fi and Bluetooth Interference. *IEEE Open Journal of the Communications Society* **2020**, *1*, 60–76.
43. Kim, B.; Khan, D.; Bohak, C.; Choi, W.; Lee, H.; Kim, M. V-RBNN Based Small Drone Detection in Augmented Datasets for 3D LADAR System. *Sensors* **2018**, *18*, 3825. <https://doi.org/10.3390/s18113825>.
44. C. Reiser. Github page. <https://github.com/creiser/drone-detection> **2020**.
45. SafeShore consortium. <http://safeshore.eu/dataset> **2020**.
46. Schumann, A.; Sommer, L.; Klatte, J.; Schuchert, T.; Beyerer, J. Deep cross-domain flying object classification for robust UAV detection. In Proceedings of the 14th IEEE International Conference on Advanced Video and Signal Based Surveillance (AVSS), 2017, pp. 1–6. <https://doi.org/10.1109/AVSS.2017.8078558>.
47. Svanström, F. Drone Detection and Classification using Machine Learning and Sensor Fusion. Master's thesis, School of Information Technology, Halmstad University, 2020.
48. RFbeam Microwave GmbH. Datasheet of K-MD2. https://www.rfbeam.ch/files/products/21/downloads/Datasheet_K-MD2.pdf **2019**.
49. Mostafa, M.; Zahran, S.; Moussa, A.; El-Sheimy, N.; Sesay, A. Radar and Visual Odometry Integrated System Aided Navigation for UAVS in GNSS Denied Environment. *Sensors* **2018**, *18*. <https://doi.org/10.3390/s18092776>.
50. Create YOLO v2 Object Detection Network. <https://se.mathworks.com/help/vision/ug/create-yolo-v2-object-detection-network.html> **2019**.
51. Motion-Based Multiple Object Tracking. <https://se.mathworks.com/help/vision/ug/motion-based-multiple-object-tracking.html> **2019**.
52. MathWorks. Classify Gender Using LSTM Networks. <https://se.mathworks.com/help/deeplearning/ug/classify-gender-using-long-short-term-memory-networks.html> **2019**.
53. Airplane Tracking Using ADS-B Signals. <https://se.mathworks.com/help/comm/ug/airplane-tracking-using-ads-b-signals.html> **2019**.
54. Sanfridsson, J.; Sparrevik, J.; Hollenberg, J.; Nordberg, P.; Djärv, T.; Ringh, M.; Svensson, L.; Forsberg, S.; Nord, A.; Andersson-Hagiwara, M.; et al. Drone Delivery of An Automated External Defibrillator – A Mixed Method Simulation Study Of Bystander Experience. *Scand J Trauma Resusc Emerg Med* **2019**, *27*.
55. Svanström, F.; Alonso-Fernandez, F.; Englund, C. A dataset for multi-sensor drone detection. *Data in Brief* **2021**, *39*, 107521. <https://doi.org/10.1016/j.dib.2021.107521>.
56. Svanström, F. DroneDetectionThesis/Drone-detection-dataset: First release. <https://doi.org/10.5281/zenodo.5500576> **2020**. <https://doi.org/10.5281/zenodo.5500576>.
57. YouTube channel "VIRTUAL AIRFIELD operated by SK678387". www.youtube.com/channel/UCx-PY5Q1Z5sJOQ9e8wvWvWQ **2020**.
58. Infinitoptics. Whitepaper on thermal DRI. <https://www.infinitoptics.com/sites/default/files/attachments/Infiniti%20DRI%20Whitepaper.pdf> **2020**.
59. Chevalier, P. On the specification of the DRI requirements for a standard NATO target. *Researchgate publication* **2016**.
60. uAvioni. Datasheet of ping20Si. <https://uavionix.com/downloads/ping20s/Ping20Si-DataSheet.pdf> **2020**.

